CELL BIOLOGY

Assembly of the asymmetric human γ-tubulin ring complex by RUVBL1-RUVBL2 AAA ATPase

Fabian Zimmermann[1]*, Marina Serna[2]*, Artur Ezquerra[1], Rafael Fernandez-Leiro[2], Oscar Llorca[2†], Jens Luders[1†]

The microtubule nucleator γ-tubulin ring complex (γTuRC) is essential for the function of microtubule organizing centers such as the centrosome. Since its discovery over two decades ago, γTuRC has evaded in vitro reconstitution and thus detailed structure-function studies. Here, we show that a complex of RuvB-like protein 1 (RUVBL1) and RUVBL2 "RUVBL" controls assembly and composition of γTuRC in human cells. Likewise, RUVBL assembles γTuRC from a minimal set of core subunits in a heterologous coexpression system. RUVBL interacts with γTuRC subcomplexes but is not part of fully assembled γTuRC. Purified, reconstituted γTuRC has nucleation activity and resembles native γTuRC as revealed by its cryo–electron microscopy (cryo-EM) structure at ~4.0-Å resolution. We further use cryo-EM to identify features that determine the intricate, higher-order γTuRC architecture. Our work finds RUVBL as an assembly factor that regulates γTuRC in cells and allows production of recombinant γTuRC for future in-depth mechanistic studies.

INTRODUCTION

Microtubules are tubular polymers of heterodimers of α- and β-tubulin. Networks of microtubules are essential for various cellular functions ranging from chromosome segregation during cell division to intracellular transport. Formation, maintenance, and remodeling of these networks crucially depend on microtubule nucleation and its regulation in space and time (*1*, *2*). Nucleation requires another type of tubulin, γ-tubulin, which interacts with members of the conserved gamma complex protein (GCP) family (*3*, *4*). Budding yeast contains only two GCPs, GCP2 and GCP3. These two proteins associate laterally, and each binds one molecule of γ-tubulin, giving rise to a heterotetrameric, "Y"-shaped γ-tubulin small complex (γTuSC) (*5*). Other eukaryotes including humans use three additional GCP family members, GCP4, GCP5, and GCP6. Higher-order oligomeric assemblies of GCPs function as nucleation templates by presenting γ-tubulin molecules in a circular, helical arrangement that resembles the configuration of α- and β-tubulin in the microtubule (*3*, *4*, *6*–*8*). In budding yeast, the nucleation template is formed by γTuSC oligomerization. This is promoted by interaction with adapter proteins at the spindle pole body, a microtubule organizing center (MTOC) that is equivalent to the animal centrosome (*9*). In the presence of a fragment of the Spc110 adapter, recombinant γTuSC can also oligomerize in vitro (*10*). However, the nucleation activity of these complexes is relatively weak. Consistent with this observation, structural analysis of helical γTuSC oligomers by cryo–electron microscopy (cryo-EM) has revealed outward displacement of GCP3-bound γ-tubulins, resulting in an imperfect nucleation template. Thus, apart from oligomerization, formation of an efficient nucleator may require an activation step that adjusts the positioning of the γ-tubulin molecules (*10*, *11*).

In contrast to budding yeast, γ-tubulin ring complexes (γTuRCs) in animal cells are found preassembled in the cytosol, raising the question of how ectopic nucleation is prevented. Recent cryo-EM structures of native γTuRC purified from cytosol have provided some insight (*12*–*14*). γTuRC was shown to be a cone-shaped complex, formed by four laterally arranged γTuSCs, followed by two γTuSC-like complexes involving GCP4-GCP5 and GCP4-GCP6 pairs, and ending with an additional γTuSC. However, the γTuSC-like subcomplexes and the final γTuSC do not follow a circular trajectory and are splayed outward, conferring an overall elliptic rather than circular shape to native γTuRC. In addition, both the lateral spacings between γ-tubulins and the pitch of the γ-tubulin helix do not match the configuration of tubulin in a microtubule. Thus, native γTuRC may be in an inactive configuration (*12*–*14*). Consistently, purified cytosolic γTuRC has only moderate nucleation activity (*13*–*16*). How the major conformational change required to match the microtubule geometry might be brought about is unclear. Adding to this, multiple densities in the native γTuRC cryo-EM maps could not be assigned, and several subunits that were present in the purified material could not be mapped. Moreover, several regions in the GCPs including the ~200– to 300–amino acid N-terminal extensions (NTEs) of GCP2, GCP3, GCP5, and GCP6 were not resolved (*12*–*14*). The NTEs of GCP3, GCP5, and GCP6 bind the small γTuRC subunit MZT1 (Mozart1), which promotes targeting to MTOCs, presumably by promoting interaction with attachment factors (*17*, *18*). For MZT1 in *Schizosaccharomyces pombe* and *Candida albicans*, this may be linked to γTuSC oligomerization and activation, but the mechanistic details remain obscure (*18*, *19*). Human MZT1 was shown to mediate interaction with the targeting factor NEDD1 (Neural Precursor Cell Expressed, Developmentally Down-Regulated 1) and with a nucleation activating, centrosomin motif 1–containing fragment of the large centrosomal scaffold protein CDK5RAP2 (CDK5 Regulatory Subunit Associated Protein 2), respectively (*17*). The γTuRC subunit MZT2 (also known as GCP8) was shown to interact with the N-terminal half of GCP2 (*18*) and to contribute to targeting of γTuRC to interphase centrosomes (*20*). Very recent structural work has identified complexes of NTEs with MZT1 and MZT2 as part of a bridging structure within the γTuRC cone and on the outer γTuRC surface, respectively (*21*). Deciphering how conformational constraints or specific structural features are linked to the regulation of γTuRC nucleation activity would require detailed mutational studies in vitro. However, the lack of recombinant γTuRC currently prevents this type of analysis.

[1]Mechanisms of Disease Programme, Institute for Research in Biomedicine (IRB Barcelona), The Barcelona Institute of Science and Technology (BIST), Baldiri Reixac 10, 08028 Barcelona, Spain. [2]Structural Biology Programme, Spanish National Cancer Research Centre (CNIO), Melchor Fernández Almagro 3, 28029 Madrid, Spain.
*These authors contributed equally to this work.
†Corresponding author. Email: ollorca@cnio.es (O.L.); jens.luders@irbbarcelona.org (J.L.)

Spatial separation of γTuRC assembly from activation, as observed in animal cells, may not only prevent uncontrolled nucleation but also provide additional means of regulation. For example, similar to the activation step, assembly of γTuRCs could be subject to specific control (*22*). This may explain why, to date, more than two decades after the discovery of γTuRC (*6*, *7*), the field has been unsuccessful in reconstituting γTuRC from recombinant proteins in vitro. Chaperones and chaperone-like proteins known to participate in the biogenesis of proteins and protein complexes also under nonstress conditions have commonly been found to copurify with γTuRC (*20*, *23*). This includes the CCT (Chaperonin containing TCP1) complex, which is required for the folding of tubulins including γ-tubulin (*24*), and RuvB-like protein 1 (RUVBL1) and RUVBL2. RUVBL1 and RUVBL2 are two closely related AAA (ATPases associated with diverse cellular activities) proteins that assemble into heterohexameric complexes with chaperone-like activity (*25*–*27*). RUVBL1 interacts with α- and γ-tubulin in coprecipitation experiments, colocalizes with microtubules at centrosomes and in the mitotic spindle, and is required for the assembly and organization of microtubules in mitosis (*28*, *29*). While the mechanisms underlying these activities have not been uncovered, the current view is that RUVBL1-RUVBL2 complexes are involved in multisubunit protein complex assembly. In this regard, RUVBL1-RUVBL2 can fulfill structural roles, for example, as essential components of chromatin-remodeling complexes such as SWR1 (SWI2/SNF2-Related 1) and INO80 (inositol auxotroph 80) (*30*, *31*), and catalytic roles, as part of the R2TP (Rvb1-Rvb2-Tah1-Pih1) complex. R2TP cooperates with the heat shock protein 90 (HSP90) chaperone in the formation, maturation, and activation of large macromolecular complexes such as RNA polymerase II or complexes formed by the family of phosphatidylinositol 3-kinase (PI 3-kinase)–like kinases including ATR (ataxia telangiectasia and Rad3-related)–ATRIP (ATR interacting protein) and mammalian target of rapamycin complex 1 (*25*, *26*).

Here, we reveal a novel role of a complex composed of RUVBL1 and RUVBL2 ("RUVBL") in promoting the assembly of γTuRC both in human cells and in a reconstituted in vitro system. Using a bottom-up approach, we define the minimal set of subunits for assembling human γTuSC and γTuRC. Our cryo-EM structure shows that recombinant γTuRC resembles the native complex. Further analysis enabled us to map novel structural features, providing new insight into the intricate architecture of this macromolecular machine. In vitro reconstitution of complex systems such as DNA replication and repair has been instrumental in determining their mechanistic basis. Similarly, our work now opens the way to detailed mutational and mechanistic studies aimed at understanding not only γTuRC-mediated microtubule nucleation but also the function of the RUVBL "assemblase."

RESULTS

The RUVBL complex is required for γTuRC integrity

To test whether the RUVBL complex may have a role in the folding or assembly of γTuRC subunits, we depleted RUVBL1 in HeLa cells by transfection of small interfering RNA (siRNA) (*32*). Western blotting indicated strongly reduced RUVBL1 levels after 72 hours (Fig. 1A and fig. S1A). RUVBL2 was codepleted, suggesting that we had disrupted the RUVBL complex. In RUVBL-depleted extracts, the levels of γ-tubulin and of several GCPs were also slightly reduced (Fig. 1A and fig. S1B). To gain further insight into the integrity of γ-tubulin complexes in RUVBL-depleted cells, we fractionated extracts on sucrose gradients and probed fractions for γTuRC core subunits by Western blotting. As expected, in control extracts, the bulk of all subunits cofractionated with a peak that corresponded to the size of γTuRC (Fig. 1, B to D; peak in fractions 7 and 8). In addition, complexes of small and intermediate sizes were observed, presumably corresponding to γTuSC and γTuSC-like complexes, respectively (Fig. 1, B to D, fractions 3 to 6) (*17*, *33*). Notably, depletion of RUVBL caused a redistribution of some subunits. Whereas GCP4, GCP5, and GCP6 were only mildly affected (Fig. 1B and fig. S1, C and D; peak in fraction 7), GCP2, GCP3, and MZT2 were partially shifted to fractions of smaller molecular weight. In control extracts, most of GCP2 and GCP3 fractionated as part of γTuRC, whereas in RUVBL1-depleted extract, the majority cofractionated with γTuSC (Fig. 1, B and C). A similar shift was observed for MZT2, which is associated with both γTuSC and γTuRC (*17*), presumably through binding to GCP2 (*18*) (Fig. 1, B and D). These specific profile changes were reproduced in multiple independent experiments (fig. S1, E to I). We concluded that the RUVBL complex is required for γTuRC integrity and may be important for linking γTuSC with subcomplexes composed of GCP4, GCP5, and GCP6.

RUVBL deficiency impairs assembly of centrosomal γTuRC

Previous work reported mitotic defects in RUVBL-depleted cells (*28*). In agreement with this, we found that depletion of RUVBL1 resulted in accumulation of mitotic cells with spindle and chromosome congression defects (fig. S1, J and K). Curiously, we also found that RUVBL1 depletion caused severe centriole duplication defects based on the quantification of centrin foci in mitotic cells. Whereas ~90% of control cells had at least two pairs of centrin foci (centrioles), one pair at each spindle pole, this was the case for only ~35% of RUVBL1-depleted cells, where the majority lacked one or more centrin foci (fig. S1, L and M). Thus, RUVBL is required for mitotic spindle assembly and progression, and for centriole duplication, processes that also require γTuRC (*17*, *34*, *35*). However, since RUVBL promotes the function of a range of different proteins and protein complexes, we sought to probe the involvement of RUVBL in regulating γTuRC more directly. Our sucrose gradient analysis suggested altered γTuRC composition after RUVBL depletion (Fig. 1, B to D). To test whether this also occurred in intact cells at MTOCs, we determined the centrosomal levels of MZT2 in control and RUVBL1-depleted cells, relative to NEDD1, which is known to localize to centrosomes independently of γTuRC (*35*, *36*). We observed that interphase centrosomes in RUVBL1-depleted cells displayed a specific reduction in the levels of MZT2 (Fig. 1, E and F). Thus, RUVBL controls the correct assembly of γTuRC at MTOCs.

Coexpression with MZT1 and MZT2 allows reconstitution of γTuSC

To study how RUVBL may promote assembly of γTuSC and MZT2 into γTuRC, we thought to reconstitute this process in vitro. We first attempted to produce recombinant γTuSC. We generated baculoviruses for expression of various subunit combinations in insect cells and affinity-purified the resulting complexes using a Twin-Strep-tag fused to the C terminus of GCP3. Coexpression of γ-tubulin, GCP2, and GCP3 was robust, but the proteins were largely insoluble, and only negligible amounts could be purified (Fig. 2A). This improved only slightly by coexpression with either MZT1 or MZT2. Notably, coexpressing all five proteins together substantially boosted solubility and yield, allowing purification of γTuSC (Fig. 2A). Purified

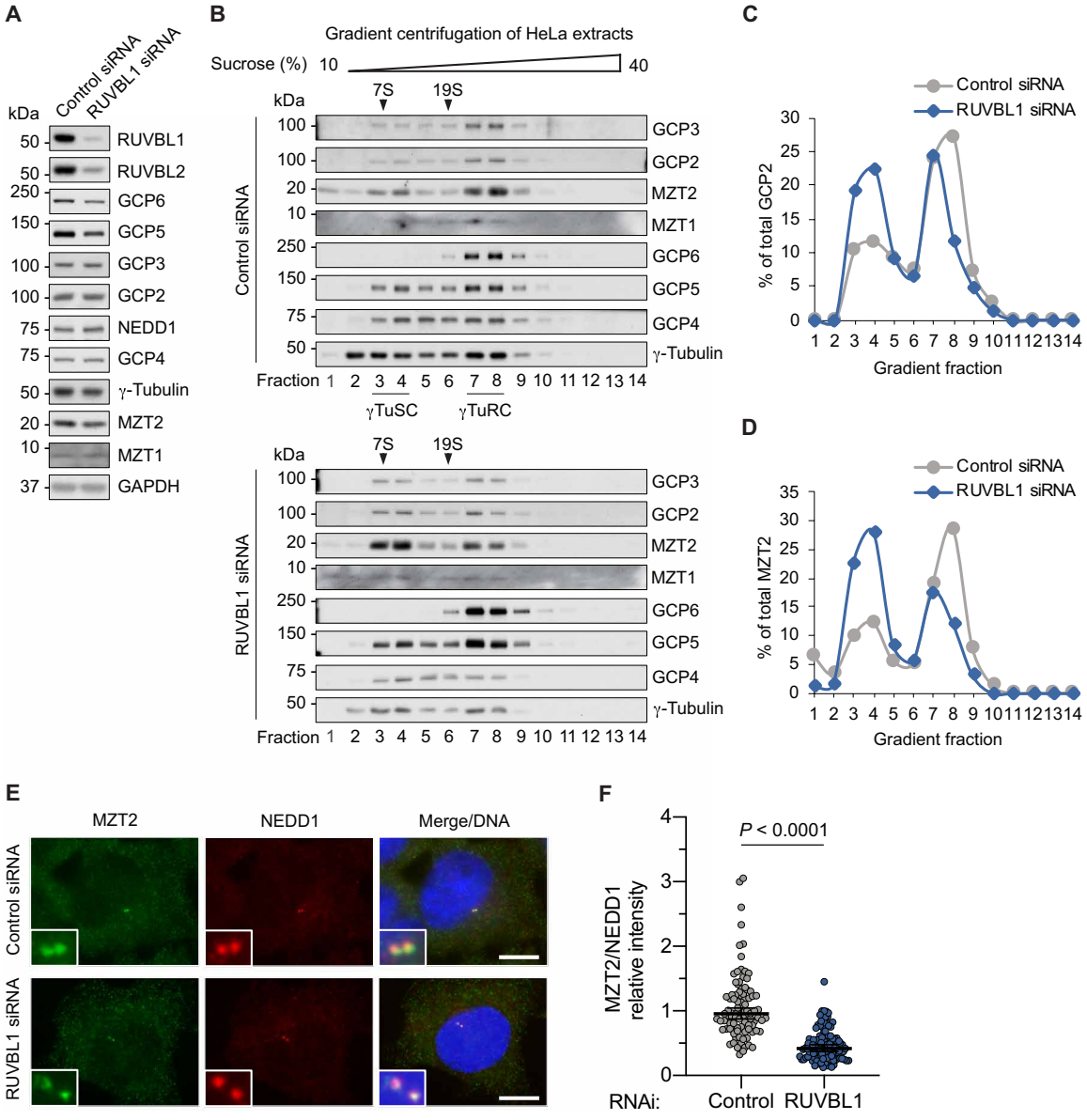

Fig. 1. RUVBL is required for γTuRC integrity in human cells. (**A**) Extracts of HeLa cells treated with control and RUVBL1 siRNA were analyzed by Western blotting with the indicated antibodies. (**B**) Extracts as in (A) were fractionated on sucrose gradients and analyzed by Western blotting. Aldolase (7S, 158 kDa) and thyroglobulin (19S, 669 kDa) served as standards. (**C**) Fractionation profiles of GCP2 in sucrose gradients shown in (B). Band intensities in fractions were quantified and plotted for control and RUVBL1-depleted extracts as indicated. Values are percentages of the sum of band intensities across all fractions. Data in (A) to (D) were reproduced in three independent experiments. (**D**) Fractionation profiles of MZT2 in sucrose gradients shown in (B) were determined as in (C). (**E**) Immunofluorescence microscopy of control and RUVBL-depleted HeLa cells after staining with anti-MZT2 and anti-NEDD1 antibodies and 4′,6-diamidino-2-phenylindole (DAPI) to stain DNA. Inset is fivefold magnified. Scale bars, 10 μm. (**F**) Fluorescence intensities for centrosomal MZT2 and NEDD1 staining as in (E) were quantified and plotted. Mean intensities were normalized to controls and plotted as fraction of MZT2 relative to NEDD1; $n = 92$ to 109 centrosomes per condition combined from two independent experiments. Bars indicate median with 95% confidence interval; $P < 0.0001$ (unpaired, two-tailed Mann-Whitney U test). RNAi, RNA interference.

γTuSC migrated at a size similar to γTuSC in cell extracts when fractionated on sucrose gradients (Fig. 2B, compare to Fig. 1B). Analysis of this material by negative-stain EM and processing of several thousands of particles revealed Y-shaped molecules (Fig. 2C). These were similar in shape to the previously described yeast γTuSC, indicating that the overall structure is conserved (*5*). In some particles, two γTuSCs were laterally associated, as would be expected for their configuration in γTuRC. Thus, coexpression with MZT1 and MZT2 allows recombinant production of assembly competent γTuSC, presumably by promoting solubility of GCP2 and GCP3.

MZT1 and MZT2 form distinct units with the NTEs of GCP3 and GCP2

Considering that MZT1 and MZT2 are not present in budding yeast and thus not required for reconstituting γTuSC of this organism (*5*),

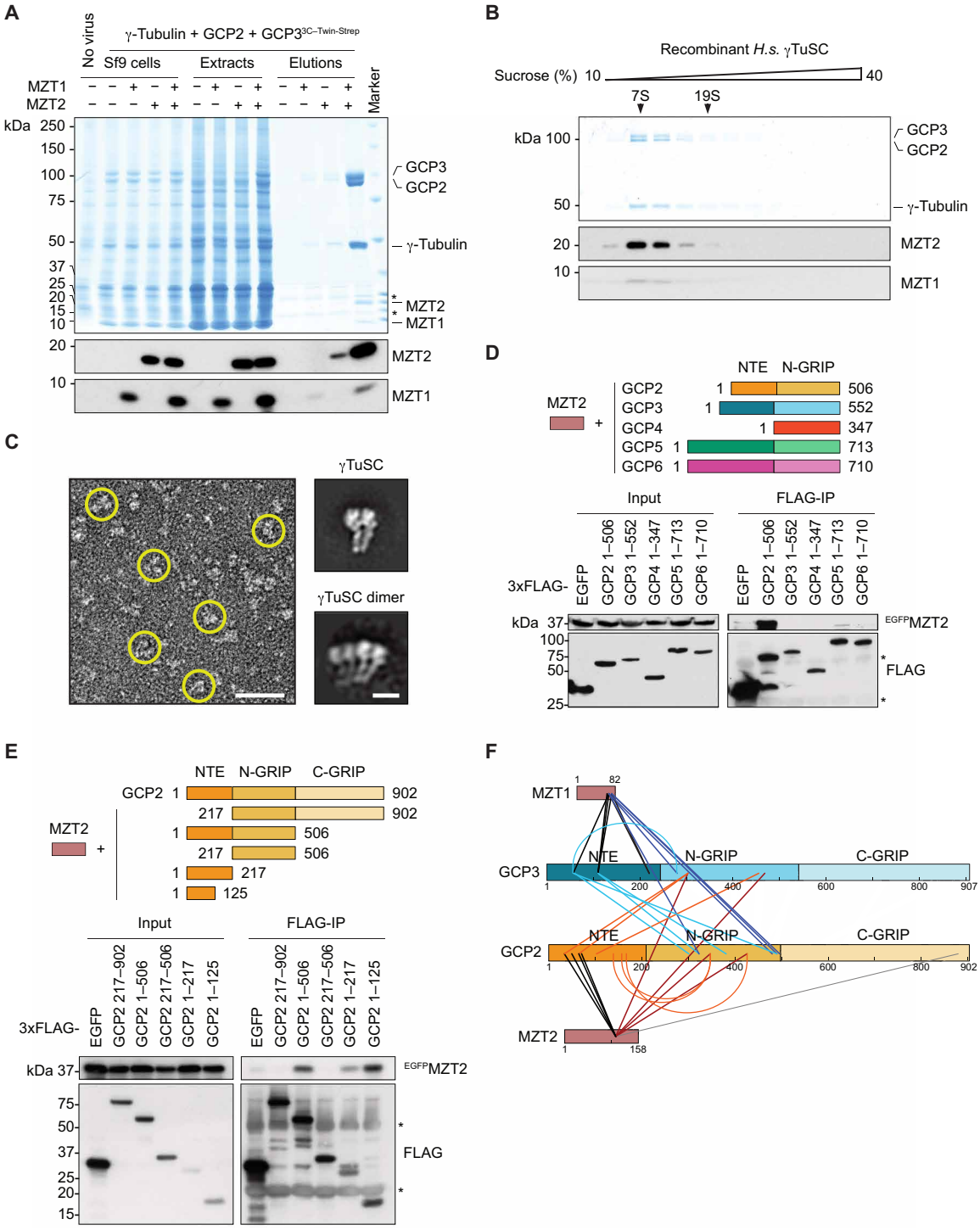

Fig. 2. MZT1 and MZT2 are required for reconstitution of human γTuSC. (**A**) Combinations of the indicated proteins were coexpressed, affinity-purified, and analyzed by SDS–polyacrylamide gel electrophoresis (PAGE). MZT1 and MZT2 were detected by Western blotting. Asterisks indicate contaminating Strep-Tactin (15 kDa) used for affinity purification and 3C protease (25 kDa) used for elution (**B**) Recombinant Homo sapiens (H.s.) γTuSC was fractionated on a sucrose gradient and analyzed as in (A). (**C**) Negative-stain EM of purified γTuSC reveals Y-shaped particles (yellow circles) (left). Scale bar, 50 nm. Two-dimensional (2D) averages of γTuSC (4489 particles) (top right) and two laterally associated γTuSCs (344 particles) (bottom right). Scale bar, 10 nm. (**D**) 3xFLAG-tagged N-terminal domains of GCP2 to GCP6 were coexpressed with enhanced green fluorescent protein (EGFP)–MZT2, immunoprecipitated (IP), and probed by Western blotting as indicated. Asterisks indicate contaminating immunoglobulin G (IgG). (**E**) 3xFLAG-tagged GCP2 fragments were coexpressed with EGFP-MZT2 and analyzed as in (D). Asterisks indicate contaminating IgG. (**F**) Cross-links of MZT1, MZT2, or the NTEs with other regions identified by CL-MS at least twice. MZT1 and GCP3-NTE were cross-linked with each other (black lines) and with the N-GRIP domains of GCP2 and GCP3 (light and dark blue lines). MZT2 and GCP2-NTE were cross-linked with each other (black lines) and with the N-GRIP domains of GCP2 and GCP3 (orange and red lines). A cross-link between MZT2 and a C-terminal loop of GCP2 is shown in gray.

we studied their interactions with γTuSC in more detail. Previous work, using yeast two-hybrid and pulldown assays, had identified the NTE of GCP3 as binding site for MZT1 (*17*, *18*, *37*, *38*). We performed a similar analysis for MZT2 by coexpressing enhanced green fluorescent protein (EGFP)–tagged MZT2 with various FLAG-tagged fragments comprising the N-terminal domains of GCPs in human embryonic kidney (HEK) 293T cells, followed by FLAG pulldown assays. This confirmed specific interaction of EGFP-MZT2 with FLAG-GCP2 1 to 506 but not equivalent fragments of other GCPs (Fig. 2D). Additional pulldowns mapped the MZT2 binding region to the first 125 amino acids in the NTE of GCP2 (Fig. 2E). Thus, in analogy to the binding of MZT1 to the NTE of GCP3, MZT2 specifically interacts with the NTE of GCP2.

To further dissect interactions between γTuSC subunits, we incubated purified reconstituted γTuSC with the cross-linker disuccinimidyl dibutyric urea (DSBU) (*39*). Analysis of these samples by SDS–polyacrylamide gel electrophoresis (PAGE) showed that increasing cross-linker concentrations caused gradual disappearance of bands corresponding to monomeric γTuSC subunits and appearance of high–molecular weight adducts (fig. S2A). Subsequent cross-linking mass spectrometry (CL-MS) identified both intra- and intermolecular cross-links (fig. S2B and table S1). Consistent with MZT1 forming a specific complex with the GCP3-NTE (referred to as MZT1:3NTE from this point on), we observed several cross-links of MZT1 with this region but not with the NTE of GCP2 (Fig. 2F, black lines). MZT1:3NTE behaved as a unit that formed multiple cross-links with more centrally located regions within the core fold of both GCP2 and GCP3 (Fig. 2F, bright and dark blue lines). In contrast and confirming the specific interaction observed in our pulldown assays, MZT2 was cross-linked to the NTE of GCP2 (referred to as MZT2:2NTE from this point on) but not the NTE of GCP3 (Fig. 2F, black lines). Similar to MZT1:3NTE, the MZT2:2NTE unit was cross-linked to more centrally located residues on GCP2 and GCP3, but these residues were different from the residues cross-linked to MZT1:3NTE (Fig. 2F, orange and red lines). Together, the data show that within γTuSC, the NTEs of GCP2 and GCP3 associate with MZT2 and MZT1, respectively, forming spatially separated units that are able to "fold back" to interact with distinct, more centrally located regions of the GCP2/3 core structure.

RUVBL associates with γTuSC

Given that, in RUVBL-depleted cells, γTuRC integrity was compromised, we asked whether RUVBL had any effect on γTuSC biogenesis. RUVBL1-RUVBL2 coexpressed with γTuSC in insect cells did not increase the yield of purified γTuSC but copurified with it (Fig. 3A and fig. S3A). To rule out that γTuSC-RUVBL interaction required other factors present in the insect cell expression host, we tested whether the interaction could be reconstituted from separately purified complexes. Similar to coexpressed RUVBL, recombinant RUVBL purified from bacteria was specifically retained on immobilized γTuSC but not on resin alone (Fig. 3B). These results show that RUVBL directly binds to γTuSC. We then sought to visualize the γTuSC-RUVBL complex using EM under mild cross-linking conditions with glutaraldehyde. When γTuSC was cross-linked in the absence of RUVBL, we observed curved γTuSC oligomers and γTuRC-like rings (Fig. 3C). These assemblies were more extensive than the γTuSC pairs observed in purified γTuSC (Fig. 2, B and C), suggesting that γTuSC has a propensity to self-associate laterally and that these transient interactions were trapped by the cross-linker. We then repeated the mild cross-linking in the presence of RUVBL. To enrich for RUVBL-γTuSC complexes, we performed pulldowns using the His-tag on RUVBL1. Negative-stain EM and two-dimensional (2D) averaging confirmed association between RUVBL and γTuSC and showed that RUVBL interacted at a specific position of the γTuSC ring (Fig. 3D). We interpreted the low-resolution (~26-Å resolution) architecture of the γTuSC-RUVBL complex by fitting the atomic structures of γTuSC and the RUVBL hexameric ring filtered at low resolution (Fig. 3, E and F). We found that RUVBL was located at a position where the two ends of the open γTuSC rings meet and that the density assigned to RUVBL could only accommodate hexameric rather than dodecameric RUVBL. Together, this analysis indicated that a hexamer of RUVBL recognizes and binds to specific structural features of γTuSC oligomers.

RUVBL1-RUVBL2 reconstitutes recombinant γTuRC

Next, we asked whether RUVBL may participate in assembling γTuRC. For this, we first tested whether coexpression of γTuSC subunits together with GCP4, GCP5, and GCP6 alone was sufficient to reconstitute γTuRC. We combined expression of γ-tubulin, GCP2, GCP3^{His6}, MZT1, and MZT2, with GCP4, GCP5, and GCP6, and moved the Twin-Strep-tag to the GCP6 subunit (GCP6$^{3C-Twin-Strep}$), to allow more specific purification of γTuRC. Using this approach, we were able to express and copurify γTuRC subunits at low yield but reasonable purity as judged by SDS-PAGE (Fig. 3G and fig. S3B). However, sucrose gradient fractionation failed to detect a defined complex corresponding to γTuRC, as judged by the broad distribution of γ-tubulin throughout all fractions and the overall poor detection of all subunits (fig. S3C). Thus, while coexpression of γTuRC subunits allows their interaction and copurification, they fail to assemble γTuRC.

We then repeated the experiment by infecting insect cells with a single baculovirus clone coexpressing all γTuRC subunits together with RUVBL1-RUVBL2. Notably, while overall expression levels were similar, the presence of RUVBL significantly increased the yield of purified γTuRC subunits, suggesting that RUVBL promoted their solubility (Fig. 3G). Notably, fractionation of this material on sucrose gradients revealed a defined peak that mirrored the fractionation of native γTuRC in cell extracts and was consistent with the expected size of ~2 MDa (Fig. 3H, compare to Fig. 1B). In agreement with a catalytic role of RUVBL in γTuRC assembly, the bulk of copurifying RUVBL1-RUVBL2 did not cofractionate with γTuRC but was present in smaller–molecular weight fractions. Negative-stain EM of the purified material revealed ring-shaped complexes confirming successful reconstitution of γTuRC (fig. S3D).

To test whether reconstituted γTuRC had nucleation activity, we incubated γTuRC with pure tubulin spiked with rhodamine-labeled tubulin in the presence of guanosine 5′-triphosphate (GTP). Reactions were stopped by chemical fixation at different time points, spotted on coverslips, and analyzed by fluorescence microscopy. At a concentration of 20 μM tubulin and 1 nM γTuRC, we observed formation of microtubules in a time-dependent manner, whereas there was no spontaneous microtubule assembly at this concentration of tubulin (Fig. 3I and fig. S3E). We conclude that coexpression of γTuRC subunits together with RUVBL1-RUVBL2 in a heterologous expression system allows efficient reconstitution and purification of human γTuRC for in vitro studies.

Reconstituted γTuRC resembles native γTuRC

To determine whether reconstituted γTuRC resembled native γTuRC, we analyzed it by cryo-EM. The purified complex was vitrified

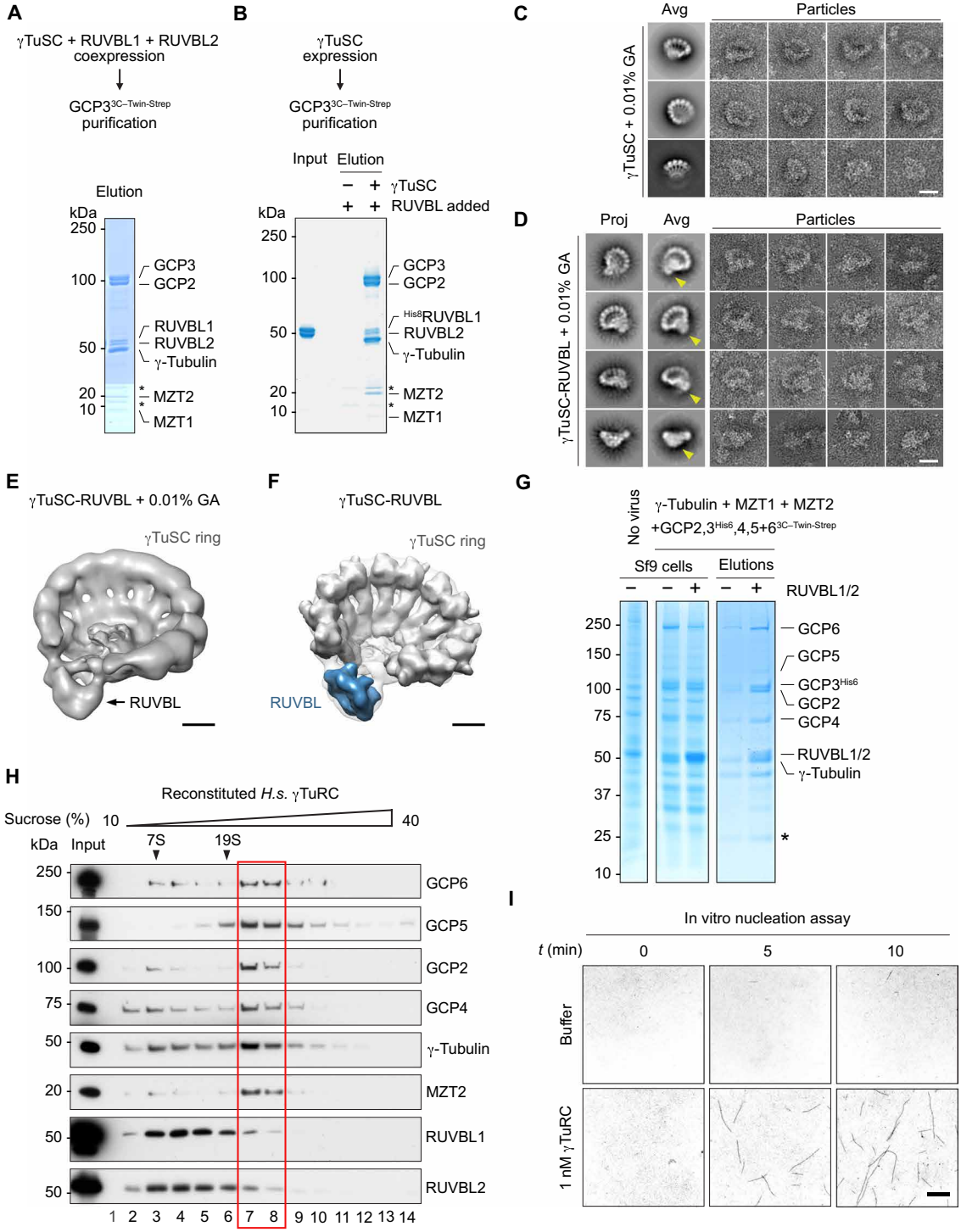

Fig. 3. RUVBL assembles subcomplexes into γTuRC. (**A**) γTuSC, coexpressed with RUVBL1-RUVBL2, was purified and analyzed by SDS-PAGE and Coomassie staining. (**B**) Purified, immobilized γTuSC was incubated with recombinant RUVBL1-RUVBL2 before elution and analysis as in (A). Asterisks denote contaminants as in Fig. 2A. (**C**) Negative-stain EM of ring-shaped γTuSC oligomers after cross-linking with 0.01% glutaraldehyde (GA). 2D averages (Avg) correspond to 1667, 1809, and 2002 particles from top to bottom. Representative particles are shown. Scale bar, 20 nm. (**D**) Negative-stain EM of reconstituted γTuSC-RUVBL complex purified after cross-linking reveals a globular density (yellow arrowheads) bound to γTuSC rings. 2D averages correspond to 213, 397, 214, and 227 particles from top to bottom and are compared to projections (proj) of the EM volume in (E). Scale bar, 20 nm. (**E**) View of negative-stain structure of γTuSC-RUVBL (~26-Å resolution). Scale bar, 5 nm. (**F**) Structure of γTuSC-RUVBL (transparent) fitted with structures of γTuSC and RUVBL1-RUVBL2 hexamer [Protein Data Bank (PDB) 2XSZ] filtered at low resolution. Scale bar, 5 nm. (**G**) γTuRC subunits coexpressed in Sf9 cells with or without RUVBL1-RUVBL2, affinity-purified, and analyzed by SDS-PAGE. (**H**) Sucrose gradient analysis of recombinant γTuRC, probed by Western blotting as indicated. Red box marks γTuRC peak fractions (compare to Fig. 1B). (**I**) Rhodamine-labeled microtubules nucleated by recombinant γTuRC were detected by fluorescence microscopy. Scale bar, 10 μM.

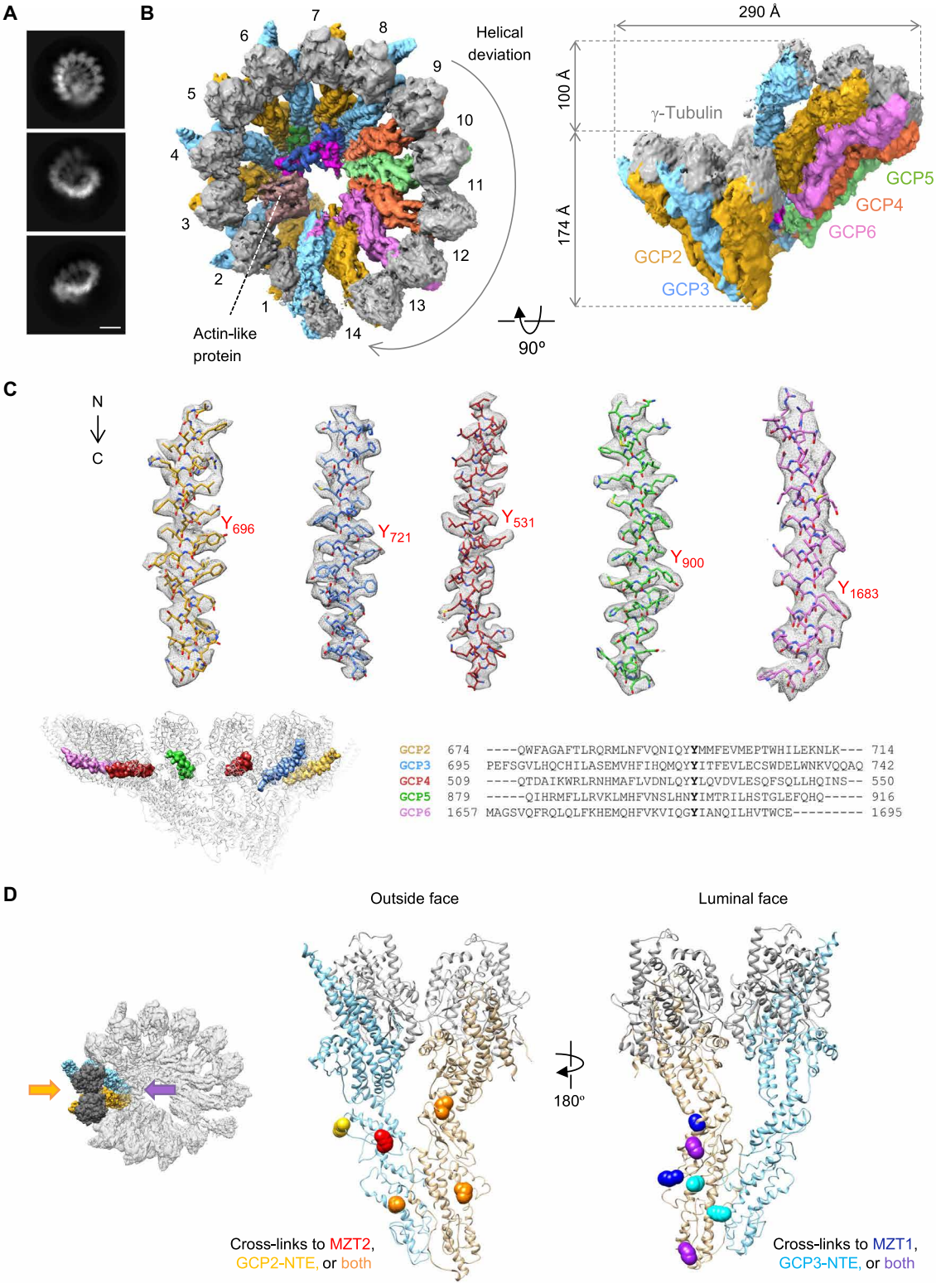

Fig. 4. Recombinant γTuRC has an asymmetric structure. (**A**) Representative 2D averages obtained from the cryo-EM images of recombinant γTuRC. The averages show the asymmetric cone-shaped structure of γTuRC. Scale bar, 10 nm. (**B**) Top and side views of the cryo-EM map for recombinant γTuRC with color-coded subunits. (**C**) Top: Cryo-EM density of a helix in GCP2, GCP3, GCP4, GCP5, and GCP6 subunits shown as mesh and with the fitted model for each subunit. The left bottom panel shows the location of each helix in the complete model of γTuRC, and the right bottom panel shows the sequences of the regions displayed. Each subunit is color-coded as in (B). (**D**) Mapping of the residues in GCP2 and GCP3 that are involved in cross-links with MZT2:2NTE and MZT1:3NTE as indicated by the color code. MZT2:2NTE maps to outside surfaces, and MZT1:3NTE maps to inside surfaces.

using holey grids with a thin carbon film placed on top. We collected cryo-EM images on a 300-kV electron microscope and selected the best particles after several cycles of 2D and 3D classification and averaging (fig. S4, movie S1, and table S2). The dataset contained views of the complex in several orientations (Fig. 4A), sufficient to determine its 3D structure at an average resolution of 4.2 Å (figs. S4 and S5). Recombinant γTuRC has the shape of a cone that is formed by 14 stalk-like units (Fig. 4B). Each unit is composed of a GCP that is bound to one molecule of γ-tubulin through its C-terminal domain. Within the cone GCPs are associated laterally mainly through their N-terminal domain, resulting in a roughly circular, helical assembly with 14 γ-tubulins presented at the open face of the cone. The GCP–γ-tubulin units at positions 9 to 14 deviate from the helical symmetry and display some degree of flexibility, reducing the resolution in this part, whereas the units at positions 1 to 8 are more rigid, resulting in significantly better resolution (Fig. 4B and figs. S4 and S5). As in the native complex, an actin-like protein is present in the lumen of the cone, although the recombinant baculovirus did not contain a corresponding expression cassette (Fig. 4B).

To deal with the conformational flexibility and to improve resolution, we used a focused refinement strategy, processing several parts of the complex independently of each other (fig. S4) (*40*). This improved average resolutions to values ranging from 3.8 to 4.0 Å. For some γTuRC subvolumes, regions in the maps reached up to 3.5-Å resolution, sufficient to model most of γTuRC (fig. S5). We identified GCP4, γ-tubulin, and the actin-like protein with the help of available crystal structures and the rest of the GCPs by unique features in their sequences in regions of high resolution, without using structural information of the native complex (Fig. 4C). As in native γTuRC, GCP2-GCP3 pairs occupy positions 1 to 8 and 13 to 14, with GCP3 displaying a distinctive, longer C-terminal hairpin structure near the γ-tubulin binding site when compared to other GCPs. The remaining positions are occupied by two γTuSC-like GCP pairs, a GCP4-GCP5 pair at positions 9/10 and a GCP4-GCP6 pair at positions 11/12 (Fig. 4, B and C).

After modeling the GCPs at all 14 positions, we compared their lateral interaction surfaces by computing total contact areas and Gibbs free energies (fig. S6A). Using these parameters as a rough readout for interaction strength, we noticed that intra-γTuSC– and intra-γTuSC–like contacts were predicted to be stronger, whereas inter-γTuSC– and inter-γTuSC–like contacts were predicted to be weaker. This would be consistent with the previous observation that high-salt treatment of extracts dissociates γTuRC into relatively salt-resistant γTuSC and γTuSC-like subcomplexes (*33*).

In addition, we identified several structural features that are also present in native γTuRC. This includes groups of bundled helices bridging the γTuRC lumen, an extended helix-hairpin structure on the inside of the cone, a globular density laterally associated with the GCP3 at position 14, and pairs of short helices situated on the outside surface of γTuSCs (*12*–*14*). We could assign several of these densities to specific proteins and also identify several new features. These findings will be presented in the following paragraphs.

We compared the atomic models of reconstituted and native human γTuRC (*12*) [Protein Data Bank (PDB) 6V6S] and quantified the root mean square deviation of the protein backbone for both models (fig. S7). This revealed high resemblance of the reconstituted and native structures with minor differences in regions found in the reconstituted complex but unresolved in the native complex and vice versa (see below).

Together, the results indicate that the presence of RUVBL1-RUVBL2 during recombinant expression promotes assembly of a complex that resembles native γTuRC and unequivocally identifies γ-tubulin, GCP2, GCP3, GCP4, GCP5, GCP6, MZT1, MZT2, and actin as the minimal set of proteins required to build the γTuRC core structure.

MZT:NTE units occupy distinct faces of the γTuRC cone

An important limitation in the cryo-EM structures of both native and reconstituted γTuRC is the lack of structural information about the majority of NTEs and their binding partners MZT1 and MZT2. To address this, we mapped the DSBU cross-linking data obtained for MZT2:2NTE and MZT1:3NTE with recombinant γTuSC (Fig. 2F) to GCP2 and GCP3 molecules within the reconstituted γTuRC structure. First, we confirmed the presence of multiple cross-links between appropriately spaced residues (*39*) when mapped on the structures of GCP2, GCP3, and γ-tubulin (fig. S8). This showed that these proteins were properly folded and assembled into γTuSC. Our previous cross-linking experiments had revealed oligomeric, ring-like particles (Fig. 3C). Consistent with this and the high–molecular weight adducts observed by SDS-PAGE (fig. S2A), DSBU also generated cross-links between GCP2 and GCP3 that would only occur upon lateral association of γTuSCs (inter-γTuSC cross-links) (figs. S2B and S8H). Notably, when we mapped the cross-links for MZT2:2NTE and MZT1:3NTE, we found that they were located on opposite surfaces on γTuSC (Fig. 4D). Whereas MZT2:2NTE cross-linked exclusively to the outside surface that γTuSC would form as part of the γTuRC cone, MZT1:3NTE cross-links were restricted to the luminal surface. Since individual residues in MZT2:2NTE and MZT1:3NTE were cross-linked to multiple residues on GCP2/3 that were distributed over an area beyond a ~25-Å radius, the maximal reach of the cross-linker, both units likely have some degree of spatial mobility.

Together, the cross-linking data revealed interactions within γTuSC and interactions that would be expected between adjacent γTuSCs as part of the γTuRC cone. In addition, the data show that MZT2:2NTE and MZT1:3NTE interact with opposite γTuSC surfaces, corresponding to the outside and inside of the γTuRC cone, respectively, where they seem to display local mobility.

MZT1:NTE units connect nonadjacent GCPs across the γTuRC lumen

Next, we sought to identify the proteins or protein parts that generated a structure composed of bundles of short helices in the lumen of reconstituted γTuRC. This structure, also referred to as "luminal bridge" (*12*), spans across from a region near the actin-like protein to a region near $GCP3_8$ and comprises two groups of bundles (Fig. 5A, bundle 1 and 2, and movie S2). In the case of our complex, only proteins used for reconstitution should participate in forming these helical densities. A good candidate was MZT1:3NTE, since our CL-MS analysis had mapped it to the γTuRC lumen. Resolution in this region was sufficient to identify three connected helices within the helical bundle 2 that matched the predicted three-helix structure of MTZ1 (Fig. 5, A and B) (*41*, *42*) and could be modeled as residues Asn^{13} to Ala^{73} of MTZ1, with an excellent agreement of the side chains with the densities in the map (Fig. 5D; helix H1 in bundle 2 shown as an example). The three MZT1 helices are intertwined with five additional helices of a different protein (Fig. 5C). Secondary structure prediction indicated that a corresponding region is present in the NTE of not only GCP3 but also GCP5 and GCP6, which all

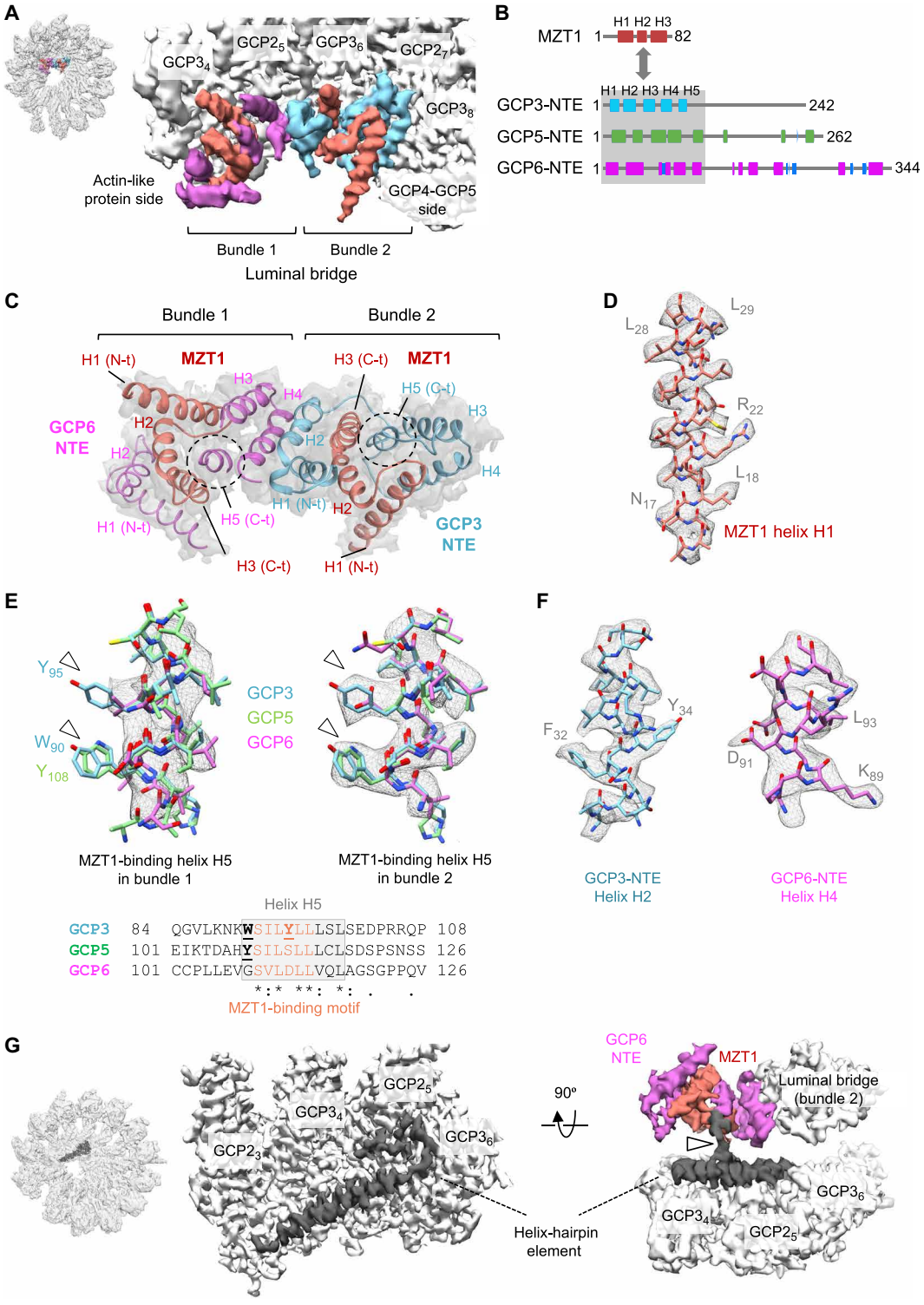

Fig. 5. Distinct MZT1:NTE units form the luminal bridge. (**A**) Two helical bundles in the γTuRC lumen that consist of two copies of MZT1 (red), GCP3-NTE (light blue), and GCP6-NTE (purple). (**B**) Secondary structure predictions for MTZ1 and the NTEs of GCP3, GCP5, and GCP6. α Helices are shown as rectangles, and β sheets are shown as blue arrows. (**C**) Model of the luminal bridge fitted into the cryo-EM map (transparent density). The three helices of each MZT1 (red) are embedded in the five-helix bundles of the GCP6-NTE (purple) and the GCP3-NTE (light blue). Dashed circles highlight helix H5 used to assign bundle 1 to GCP6 and bundle 2 to GCP3. N-terminal (N-t) and C-terminal (C-t) ends are indicated. (**D**) Model of helix H1 of MZT1 in bundle 2 fitted into the cryo-EM map. (**E**) Cryo-EM density of helix H5 fitted with GCP3, GCP5, and GCP6 sequences. For bundle 1, arrowheads point at incompatible side chains in GCP3 and GCP5, whereas GCP6 fits well. For bundle 2, prominent side chains only agree with GCP3. Bottom: Sequence alignment of H5 and the MTZ1-binding motif (*17*) in GCP3, GCP5, and GCP6. (**F**) Examples of modeled helices after protein assignment as in (E). (**G**) A helix-hairpin element in the γTuRC lumen connects adjacent γTuSCs and is linked with luminal bridge bundle 1 (arrowhead).

share a MTZ1-binding motif in predicted helix H5 (Fig. 5, B and E) (*17*). However, considering residues with bulky side chains in this region, only GCP3 showed a good fit with the density map (Fig. 5E). Following this assignment, we were able to build a model also for the remaining helices in good agreement of the side chains with the cryo-EM density (Fig. 5F). We did not detect clear connections between bundle 2 and the γTuRC ring, but subunits $GCP3_6$ and $GCP3_8$ would be sufficiently close (Fig. 5A).

We identified a second, almost identical three-helix MZT1 peptide as part of the luminal bridge bundle 1 near the actin-like protein (Fig. 5, A and C). After a roughly 180° rotation, the structure of this region matched very closely the structure of bundle 2 described above. In this case, however, MZT1 was not partnered with GCP3. Again, we compared the fit of the MTZ1-binding motifs in helix H5 of GCP3, GCP5, and GCP6 with the cryo-EM density, and only GCP6 side chains were in good agreement with the density map (Fig. 5E). Following this assignment, the model for the remaining helices also showed good agreement with the cryo-EM density (Fig. 5F).

A helix-hairpin structure beneath the actin-like protein, which is associated with the inner surfaces of GCP2/3 at positions 3, 4, 5, and 6 and was also observed in the lumen of native γTuRC (*12*), connects with bundle 1 of the luminal bridge (Fig. 5G). This is consistent with the possibility that the helix-hairpin structure corresponds to a segment of the GCP6-NTE. Together, our findings show that the luminal bridge in reconstituted γTuRC is constructed as in native γTuRC: a modular assembly composed of two distinct MTZ1:NTE units that connect nonadjacent GCPs across the γTuRC lumen.

GCP2 and GCP3 are stapled together by the NTE of GCP2

After assigning MZT1:NTEs to the γTuRC lumen, we turned our attention to previously unassigned densities on the outside of the γTuRC cone. Here, the native and reconstituted structures display so-called staples (*12*), small helical densities between GCP2 and GCP3 subunits at positions 1/2, 3/4, 5/6, 7/8, and 13/14, near the "intra-γTuSC" interfaces (Fig. 6, A and B, and movie S3). Previous work proposed that these may correspond to γTuNA (γ-tubulin nucleation activator), a small fragment of CDK5RAP2 that was used to purify native γTuRC (*12*), the NTE of GCP2 (*12*), or MZT2 (*13*), but direct evidence was missing. Again, in our recombinant complex, we could exclude proteins other than those used for reconstitution. MZT2 and the GCP2-NTE that we had mapped to the outside surface of γTuSC (Fig. 4D) were the best candidates. MZT2 is predicted to contain four helices, but only helices H2, H3, and H4 lie in the evolutionary conserved region (Fig. 6C) (*20*). In some species such as bees, MZT2 is similar in size to MZT1 and composed of only three helical segments (Fig. 6C). The MZT2-binding region in the GCP2-NTE contains six predicted helices, similar to the NTEs of GCP3, GCP5, and GCP6 (Figs. 5B and 6C). Bee GCP2 shares the predicted helical segments with human GCP2, whereas in flies, which lack MZT2, this is not the case (Fig. 6C). Together, these observations suggest that MZT2:2NTE may share structural similarity with MZT1:NTE units, which would exclude it from forming the staples. C-terminal to the MZT2-binding region, the GCP2-NTE contains two additional predicted helical segments (Fig. 6C). Examination of this region allowed us to unambiguously assign residues 150 to 188 of the GCP2-NTE to the two arms of the staple (Fig. 6D) and residues 189 to 209 to the density that connects the staple to the N terminus of the GCP2 core fold (Fig. 6, B and D). This assignment is also supported by our γTuSC cross-linking data. We found cross-links of residues K157 and K167 in the region that we assigned to the staple, with residues on the outer surface of GCP2 that surrounded the staple (Fig. 6E).

As noted previously, the region occupied by the staple at the GCP2-GCP3 interface is bound to Spc110 in yeast γTuSC (*13*). The NTE of yeast GCP2 lacks a region corresponding to the staple. Instead, a sequence resembling the staple sequence in human GCP2 is present in a segment of Spc110 (Fig. 6F). Thus, the NTE of human GCP2 and a segment of yeast Spc110 may share binding determinants needed to recognize the region at the interface of GCP2 and GCP3.

A notable feature of the staple is its position. Placed at the interface between GCP2/GCP3 within each γTuSC, one staple arm contacts the N-terminal gamma ring protein (GRIP) domain of GCP2, the other the N-terminal GRIP domain of GCP3 (Fig. 6B). A comparison of the computed contact surfaces between $GCP2_3$/$GCP3_4$ with and without staple reveals that the staple contributes ~40% of the total contact area (fig. S6B), identifying the GCP2-NTE as an important stabilizer of lateral GCP contacts.

Extended helical features connect adjacent GCPs

Apart from the GCP-NTEs and MZT:NTE entities, several additional, mostly helical elements appear to connect adjacent GCPs, potentially stabilizing the γTuRC structure. The first, a helix-hairpin motif, was already mentioned above in the context of the luminal bridge. Part of this element is a long helix that extends across and links the N-terminal GRIP domains of $GCP2_3$, $GCP3_4$, $GCP2_5$, and $GCP3_6$ (Fig. 5G). A second, likely stabilizing element was observed at the bottom of the γTuRC cone near the N-terminal GRIP domains of $GCP5_{10}$, $GCP4_{11}$, and $GCP6_{12}$ (Fig. 7A). We could not assign this element to specific subunits, but it establishes contacts with the core folds of all three of the above GCPs, suggesting that it might stabilize their lateral association (Fig. 7A).

In addition, we found a previously undescribed helical "zig-zag" element connecting the N-terminal GRIP domains of $GCP6_{12}$, $GCP2_{13}$, and $GCP3_{14}$ on their luminal side (Fig. 7A). This feature pointed in the direction of a globular density that protruded laterally from GCP3 at position 14 (described further below), but we did not observe a direct link. These helices could correspond to parts of the long GCP6 insertion or to the NTE of GCP5 (see below). In summary, multiple helical elements transversally connect adjacent GCPs in the γTuRC ring, likely contributing to the assembly and/or stability of the complex.

Additional elements near the seam of the γTuRC cone

A novel feature not described in native γTuRC was found in association with GCP6. GCP6 contains a large, >800–amino acid insertion between the N- and C-terminal GRIP domains, which has not been modeled because of the lack of corresponding density in the available cryo-EM maps. We have sufficient resolution to identify three long helices on the luminal side of GCP6 that belong to the C-terminal end of this insertion (Fig. 7, A and B). The most C-terminal helix (H3, residues 1484 to 1510) connects to the C-terminal GRIP domain of GCP6 and was also identified in the structure of human native γTuRC (Fig. 7B, inset) (*12*). Our structure now reveals a clear continuity with two additional helices that had not been observed before and that we identified by modeling as residues Glu^{1415} to Ser^{1475} (Fig. 7B, helices H2 and H3). The N-terminal end of H1 reaches up to γ-tubulin and is positioned very close to the surface of γ-tubulin that is in contact with α-tubulin during nucleation.

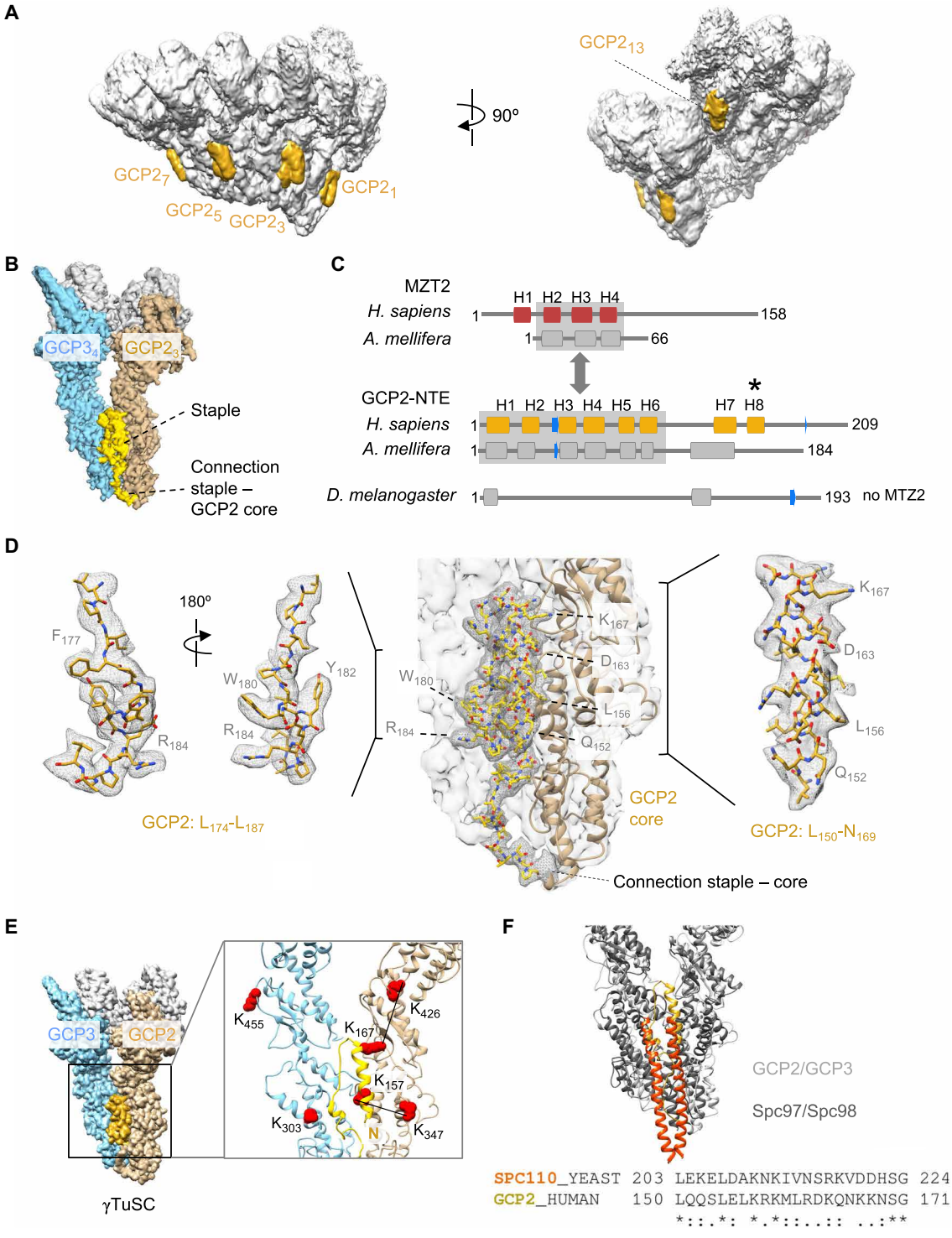

Fig. 6. GCP2-NTEs staple GCP2 and GCP3 subunits within γTuSC. (**A**) Views of recombinant γTuRC at low contour level with staples highlighted in yellow. (**B**) The staple at the interface of GCP2$_3$ and GCP3$_4$ connects to the GCP2 core (shown in yellow). (**C**) Secondary structure predictions for MTZ2 and GCP2-NTEs from several species using JPred4 (*64*). α Helices are indicated as rectangles, and β sheets are indicated as blue arrows. The asterisk marks the region of the staple. (**D**) Close-up view of the modeled staple, the density that connects staple and GCP2 core fold, and the adjustment of the atomic model to the cryo-EM map. Prominent side chains are indicated. (**E**) Mapping of cross-links between staple and N-terminal GRIP domain of GCP2 (black lines) as identified by CL-MS. GCP3 residues cross-linked with residues near the staples that were not modeled are also highlighted. (**F**) Superposition of the structures of GCP2-GCP3 from reconstituted γTuRC and yeast γTuSC bound to Spc110 (PDB 5FLZ). Spc110 and the staple partially overlap and show similarities in their primary sequence (bottom).

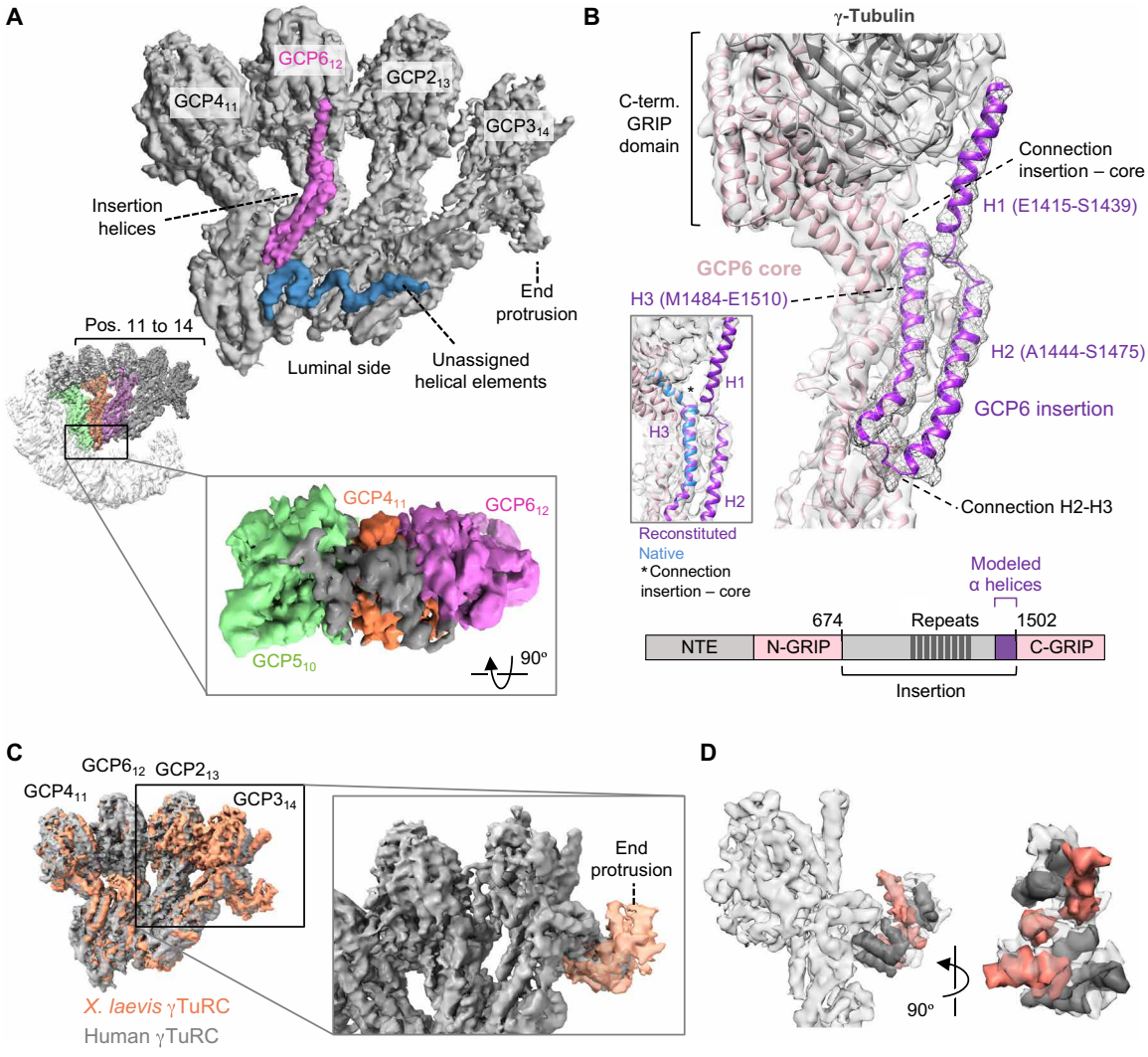

Fig. 7. The cryo-EM structure of recombinant γTuRC reveals new features near the seam. (**A**) Top: Cryo-EM densities for helical elements on the luminal side of γTuRC. Helices assigned to GCP6 are shown in purple, and unassigned helices are shown in blue. Bottom: Unassigned helical densities (gray) contact GCPs at positions 10, 11, and 12. (**B**) Three long GCP6 helices (purple), named H1 to H3 as indicated, were identified as part of the large insertion between the N- and C-terminal GRIP domains. H3 was already modeled in native γTuRC (blue) and connects to the C-terminal GRIP domain of GPC6. The bottom schematic indicates the location of the modeled helices within the long GCP6 insertion. (**C**) Superposition of the regions displaying the end protrusion in recombinant human γTuRC (gray) and native γTuRC from *X. laevis* (orange). (**D**) Fitting of a MZT1:3NTE unit (MZT1 helices in red and 3NTE helices in dark gray) to the end protrusion of *X. laevis* γTuRC.

The preceding, much larger portion of the insertion was not found in the cryo-EM map, but it is tempting to speculate that it may be able to influence events occurring at the nucleation interface.

A structural feature that we named "end protrusion" was also observed in native γTuRC but was left unassigned. Subsequently, it was proposed to be composed of a MZT:NTE-like module (*21*). The density extends laterally from the C-terminal half of GCP3 at position 14 and is not present in GCP3s at other positions (Fig. 7A). The flexibility at position 14 did not provide sufficient resolution for modeling. However, the corresponding density is relatively well defined in native γTuRC from *Xenopus laevis* (Fig. 7C) (*14*). Closer examination revealed notable similarity with the helical bundles described above for the luminal bridge, composed of three MZT1 helices and five surrounding helices (Fig. 7D). Since the single copy of MZT1:6NTE in γTuRC is part of the luminal bridge, the end protrusion should be composed of either MZT1:3NTE or MZT1:5NTE. Given that we found MZT1:3NTE to be cross-linked to the luminal side and almost exclusively to GCP2 (Fig. 4D) and that GCP5 forms MZT1:5NTE complexes but they have not been found as part of the luminal bridge, the end protrusion may be formed by the single MZT1:5NTE unit present in γTuRC.

DISCUSSION

Here, we present the reconstitution and purification of human γTuRC using baculovirus-mediated coexpression in insect cells. Building the γTuRC structure required eight recombinant proteins, γ-tubulin, GCP2–6, MZT1, and MZT2. In addition, an actin-like protein was incorporated nonrecombinantly, provided by the expression host. However, these nine proteins did not readily assemble into γTuRC but required coexpression of the RUVBL assemblase composed of RUVBL1 and RUVBL2. RUVBL was not part of the final γTuRC

structure but catalyzed the productive assembly of its subunits. This result may explain why, despite the identification of all required subunits many years ago, reconstitution has not been achieved previously. In the course of these experiments, we also succeeded in reconstituting human γTuSC. In contrast to budding yeast γTuSC, formation of the human complex required coexpression of MZT1 and MZT2. This is the first demonstration that nonyeast proteins are able to assemble stable γTuSC, supporting the view that in animal cells, γTuSC and γTuRC may coexist.

The requirement for RUVBL in γTuRC assembly was observed not only in the reconstitution system but also in human cells, where it may serve as a regulatory mechanism. RUVBL-depleted cells displayed severe mitotic spindle defects, consistent with previous reports (*28*). Unexpectedly, we also observed impaired centriole duplication after RUVBL depletion. While these phenotypes may result from impaired γTuRC integrity (*17*), γTuRC was not completely disrupted, and we suspect involvement of additional RUVBL substrates. RUVBL depletion interfered specifically with the incorporation of γTuSC and MZT2. Apart from providing essential structural support to GCP2-NTE, the cellular roles of MZT2 are poorly understood. Thus, the functional consequences of RUVBL-dependent alterations in γTuRC composition remain to be determined.

Using cryo-EM analysis, we showed that reconstituted γTuRC resembles native γTuRC isolated from human or frog cell extract. As native γTuRC, it has nucleation activity but displays an asymmetric structure that deviates from the circular geometry of a microtubule end. Thus, assuming a template nucleation mechanism, major conformational changes may be required to stimulate γTuRC nucleation activity. Alternatively, these changes may be brought about passively once a microtubule has formed on γTuRC (*43*). In this case, nucleation activity may not be stimulated by a conformational change in γTuRC but at the level of the nascent microtubule, by stabilizing factors or by the local availability of α-β-tubulin heterodimers. Our reconstituted γTuRC provides a valuable new tool for addressing these questions in the future.

The GCP-NTEs and MZT1 and MZT2 play central roles in γTuRC assembly. MZT1 forms structurally similar but distinct units with the NTEs of GCP3, GCP5, and GCP6, whereas MZT2 forms a unit with the NTE of GCP2. One MZT1:3NTE and one MZT1:6NTE form the luminal bridge, suggesting that distinct units can be used in a combinatorial fashion. This conclusion was also reached after further refinement of the native human γTuRC structure and x-ray structure determination of recombinant MZT1:6NTE (*12*) and of MZT1:3NTE and MZT1:5NTE (*44*). The intercalated configuration of helices belonging to two different polypeptides in MZT:NTE units may be crucial for the biogenesis and stability of the involved proteins. Production of soluble, recombinant γTuSC strongly depended on coexpression with both MZT1 and MZT2. Similar observations were previously made for recombinant expression of GCP2/3 and MZT1 in fission yeast (*19*). Our cross-linking experiments with recombinant γTuSC suggested that MZT1:3NTE and MZT2:2NTE, despite displaying some mobility, were restricted to the inside and outside of the γTuRC cone, respectively. Previous CL-MS analysis of purified γTuRC using a different cross-linker is also consistent with the presence of MZT1:3NTE and MZT2:2NTE units and with MZT2 occupying the outer surface of the γTuRC cone (*13*). We obtained structural evidence that MZT:NTEs stabilize γTuRC. As part of the luminal bridge, MZT1:3NTE and MZT1:6NTE connect nonadjacent GCPs. Despite the presence of multiple GCP3 copies, additional MZT1:3NTEs were not observed, possibly because of their mobility. If present, then they could mediate additional interactions within γTuRC or with other factors. One of the MZT1:NTEs likely forms the end protrusion (*21*). On the basis of our and previous data, we propose that the end protrusion is formed by a single MZT1:5NTE, but further analysis is needed for a firm assignment. The lateral association of the end protrusion with $GCP3_{14}$ may indicate a specific function at the seam of the γTuRC cone.

Our CL-MS data showed engagement of MZT2:2NTE modules on the outside of the γTuRC cone, near the staple elements. While we were unable to find MZT2:2NTE modules in the cryo-EM map, we could assign an adjacent region in the GCP2-NTE to the staple elements. Apart from stabilizing the intra-γTuSC interface, each staple with its adjacent MZT2:2NTE unit would be suited for interactions with other, potentially regulatory factors. A MZT2:2NTE unit was proposed to interact with γTuNA peptides at the outside surface of $GCP2_{13}$ (*21*).

Apart from MZT1:NTE and MZT2:2NTE modules, we identified additional, likely stabilizing features. The first, a luminal helix-hairpin element, runs across the N-terminal GRIP domains of $GCP2_3$, $GCP3_4$, $GCP2_5$, and $GCP3_6$ and is additionally linked with MZT1:6NTE of the luminal bridge, suggesting that it may be part of the GCP6-NTE. This was found to be the case in native γTuRC (*21*). The second element connects the N-terminal GRIP domains of the adjacent $GCP5_{10}$, $GCP4_{11}$, and $GCP6_{12}$ at their bases, which could explain the stability of a GCP4/5/6 subcomplex observed after salt-mediated γTuRC disruption (*33*). A third, newly identified helical zig-zag element runs along the inner N-terminal surfaces of $GCP6_{12}$, $GCP2_{13}$, and $GCP3_{14}$. This element could also be part of the GCP6-NTE or of the large GCP6 insertion, preceding the three C-terminal helices that we have assigned to this region. Alternatively, it may be formed by the NTE of GCP5. If the end protrusion is built by a MTZ1:5NTE unit (see above), then these zig-zag helices may connect it with the GCP5 N-terminal GRIP domain. Last, the remaining pair $GCP2_1$/$GCP3_2$ is engaged with the luminal actin-like protein, which, in turn, is in contact with the luminal bridge.

The extensive interconnections between GCPs suggest that γTuRC assembly and stability may not primarily depend on lateral interactions between GRIP domains but also on hitherto underappreciated interactions of less conserved GCP regions and accessory proteins. Consistently, recombinant γTuSC had a propensity to self-associate but formed γTuRC-like rings only in the presence of cross-linker. The staples at the intra-γTuSC interfaces are unlikely to affect ring formation directly but may do so indirectly, by ensuring γTuSC integrity.

A well-characterized role of RUVBL is to promote assembly of protein complexes such as RNA polymerases and PI 3-kinase-like kinases, by serving as a platform that brings client proteins together with the HSP90 chaperone (*27*, *45*). However, in other cases, RUVBL also promotes protein complex assembly in the absence of HSP90, but how this is achieved is still mysterious. Our in vitro reconstitution system now provides an ideal model for tackling this issue. Some RUVBL copurified with reconstituted γTuRC but was not a stoichiometric component. Instead, it could associate with subcomplexes such as γTuSC. However, γTuSC did not require RUVBL for its own assembly. We hypothesize that RUVBL has a role in allowing γTuSC and γTuSC-like protomers to assemble into the higher-order γTuRC structure. Liu *et al.* (*14*) proposed that GCP4, GCP5, and GCP6 may form a platform, onto which multiple γTuSC assemble. Consistent with such a model, depletion of RUVBL in cells impaired incorporation

of γTuSC into γTuRC. RUVBL may facilitate the various interconnections among GCPs that stabilize their lateral association. Dissecting the interactions of RUVBL and γTuRC subunits in vitro, in combination with structural studies, should allow unraveling the mode of action of the RUVBL assemblase.

The lack of recombinant γTuRC has hampered progress in understanding the nucleation mechanism for decades. Our current knowledge is derived almost entirely from studies of recombinant yeast γTuSC and in vitro–generated γTuSC oligomers with limited resemblance to γTuRC. Using RUVBL-mediated assembly, we have been able to overcome this limitation. Using recombinant γTuRC and γTuRC mutants in recently established single-molecule, total internal reflection fluorescence microscopy–based nucleation assays (*13*, *43*) now paves the way for exciting new discoveries in the near future.

MATERIALS AND METHODS

Cloning and plasmids

Plasmids for baculovirus-mediated expression in insect cells were generated using the biGBac system (*46*). Sequences of full-length γ-tubulin (TUBG1), MZT1, MZT2B, GCP2, GCP3, GCP4, GCP5, GCP6, RUVBL1, and RUVBL2 were inserted into pLIB. GCP3^{His6} contains a C-terminal His-tag preceded by a Gly linker (GCP3-GG-GGGG-HHHHHH). GCP3$^{3C–Twin\text{-}Strep}$ and GCP6$^{3C–Twin\text{-}Strep}$ contain a C-terminal Twin-Strep-tag preceded by an Ala-Ser linker and an HRV (human rhinovirus) 3C cleavage site (AS-LEVLFQGP-SSWSHP QFEKGGGSGGGSGGGSSWSHPQFEK). Multiple gene expression cassettes from pLIB vectors were cloned into pBIG plasmids using Gibson Assembly. Clonings were verified by sequencing.

For expression of 3xFLAG-tagged GCP2 fragments in HEK293T cells, the corresponding regions were amplified by polymerase chain reaction (PCR) and cloned into a pCS2^{+}-based vector carrying an N-terminal 3xFLAG tag and a modified cloning site with Fse I and Asc I restriction sites. All plasmids are listed in table S3.

Cell culture and treatments

HeLa and HEK293T cells were grown in Dulbecco's modified Eagle's medium + 10% fetal calf serum at 37°C and 5% CO_2. HeLa cells were transfected with Luciferase control siRNA (Thermo Fisher Scientific) or RUVBL1 siRNAs (*32*) using Lipofectamine RNAiMAX (Life Technologies) and analyzed after 68 to 72 hours. HEK293T cells were transfected with plasmids using Lipofectamine 2000 (Life Technologies) and harvested after 24 hours. For immunofluorescence microscopy, cells were grown on poly-D-lysine–coated coverslips and fixed with either 3.6% paraformaldehyde (Sigma-Aldrich) at room temperature or ice-cold methanol. For baculovirus-mediated expression, Sf9 cells (Thermo Fisher Scientific) were grown in suspension in Sf-900 III SFM (Gibco) at 27°C, at 120 rpm with 25-mm shaking throw.

Sucrose gradient centrifugation

Phosphate-buffered saline (PBS)–washed HeLa cell pellets were lysed in buffer A [50 mM Hepes (pH 7.2), 150 mM NaCl, 5 mM $MgCl_2$, 1 mM EGTA, 0.5% IGEPAL CA-630, 2 mM β-mercaptoethanol, 2× EDTA-free protease inhibitors (Roche), and 1× PhosSTOP phosphatase inhibitors (Roche)] on ice. Extracts were cleared by centrifugation for 20 min at 16,100*g* at 4°C. Protein concentration was determined by Bradford assay (Bio-Rad) and adjusted with buffer A. Extract or purified protein sample (250 μl) was loaded onto a 4.2-ml 10 to 40% linear sucrose gradient prepared in buffer B (without IGEPAL CA-630, protease inhibitors, and phosphatase inhibitors) or buffer E (described below), respectively. Centrifugation was carried out using an MLS-50 rotor at 50,000 rpm for 4 hours at 4°C. Three hundred microliters of fractions was collected by pipetting from top to bottom.

Immunofluorescence microscopy

Fixed cells on coverslips were washed with PBS, blocked, and incubated with antibodies as indicated in PBS-BT (PBS, 3% bovine serum albumin, and 0.1% Triton X-100) for 30 min at room temperature, separated by washed with PBS-BT. DNA was stained with 4′,6-diamidino-2-phenylindole (DAPI; 0.5 μg/ml) in PBS-BT, and coverslips were mounted on glass slides using ProLong Gold Antifade (Thermo Fisher Scientific). Immunofluorescence microscopy was performed using a DMI6000B microscope (Leica) with 1.4–numerical aperture (NA) 63× and 100× oil immersion objectives. Images acquired with constant exposure settings were processed, and fluorescence intensities were quantified and background-corrected with ImageJ software. The following antibodies were used: rabbit anti-MZT2 (*20*), mouse anti-NEDD1 (7D10, Sigma-Aldrich); mouse anti–α-tubulin (DM1A, Sigma-Aldrich), and mouse anti-centrin (20H5, Sigma-Aldrich). Alexa Fluor 488 and Alexa Fluor 568 secondary antibodies were purchased from Thermo Fisher Scientific.

Bacmid and bacoluvirus generation

Bacmids were generated by Tn7 transposition of pBIG2-based constructs into the EMBacY baculovirus genome as described (*46*). Baculoviruses were generated as described (*47*) with minor modifications. Briefly, bacmid DNA diluted in sterile-filtered PBS was mixed with 40-kDa linear polyethylenimine (PEI) (Polysciences) (pH 7.0) at a ratio of 1:2 (w/w) (1 μg of bacmid DNA per 1 ml of Sf9 culture). DNA:PEI complexes were allowed to form for 20 to 25 min at room temperature and added dropwise to 15 to 25 ml of Sf9 cells at culture (10^6 cells/ml). After culturing for 5 days at 27°C, the fraction of infected, yellow fluorescent protein (YFP)–positive Sf9 cells was determined using an Eclipse Ts2 microscope (Nikon). When >90% of Sf9 cells were YFP-positive, P_0 virus was harvested by pelleting at 300*g* for 5 min. The supernatant was passed through a 0.2-μm syringe filter (GE Healthcare) and stored at 4°C without further virus amplification.

Baculovirus-mediated protein expression in insect cells

P_0 virus was used to infect Sf9 cultures at 10^6 cells/ml at a ratio of 1:100 (v/v). After 68 to 72 hours of incubation at 27°C, cells were pelleted at 300*g* for 5 min, washed with PBS, either used directly for purification or snap-frozen in liquid nitrogen, and stored at −80°C.

Protein complex purification

γ-Tubulin small complex

Insect cell pellets with γTuSC containing GCP3$^{3C–Twin\text{-}Strep}$ were resuspended in 5 ml of buffer C [50 mM tris (pH 8.0), 200 mM NaCl, 1 mM $MgCl_2$, 1 mM EGTA, 2 mM β-mercaptoethanol, 0.1% IGEPAL CA-630, and 2× EDTA-free protease inhibitors] per gram of cell pellet, lysed in a dounce tissue grinder (Sigma-Aldrich) with 20 strokes on ice, and centrifuged for 25 min at 20,000*g* at 4°C. Cleared cell extracts, supplemented with 2.5 mg of avidin (E-proteins) and 625 U Universal Nuclease (Pierce) or Denarase (c-LEcta) per 10 ml of extract, were incubated 5 min on a tube roller mixer at 4°C.

γTuSC was bound by gravity flow to Strep-Tactin XT (IBA Lifesciences) resin equilibrated in buffer D (buffer C without IGEPAL CA-630 and EDTA-free protease inhibitors) (1 ml of resin per liter culture) and washed with 10 column volumes (CV) of buffer D + 0.1 mM GTP (Carbosynth) and subsequently with 10 CV of buffer E [buffer D containing Hepes (pH 7.5) instead of tris (pH 8.0)] + 0.1 mM GTP. To elute γTuSC, the resin was resuspended in 1.5 to 2 CV of buffer E + 0.1 mM GTP and digested with 100 μg of 3C protease per 1 ml of resin for 12 to 16 hours on an incubator wheel at 5 to 7 rpm at 4°C. His-tagged 3C protease was removed by gravity flow over 50 μl of Ni Sepharose (GE Healthcare) equilibrated in buffer E + 0.1 mM GTP. Purified γTuSC was centrifuged at 16,100*g* for 10 min at 4°C, concentrated using Vivaspin 500 devices with 30-kDa molecular weight cutoff (MWCO) (Sartorius), and centrifuged again as before. For storage, aliquots at 2.8 to 4.5 mg/ml were snap-frozen in liquid nitrogen and transferred to −80°C. The typical yield was ~1 mg of γTuSC per 1 liter of expression culture.

RUVBL1-RUVBL2

Recombinant RUVBL1-RUVBL2 complex was purified as described (*48*).

γTuSC-RUVBL1-RUVBL2

Purification was performed from Sf9 cells coexpressing γTuSC and RUVBL subunits as described for γTuSC but omitting removal of 3C protease. Alternatively, γTuSC and RUVBL1-RUVBL2 were purified separately and subsequently combined. For this, γTuSC was first purified from a 1-g insect cell pellet as described above. After γTuSC binding to 0.25 ml of Strep-Tactin XT, the resin was washed and resuspended in 3 CV of buffer E + 0.1 mM GTP. Purified recombinant ^{His6}RUVBL1-RUVBL2 (250 μg) was mixed with either 0.25 ml of γTuSC-bound or control Strep-Tactin XT resin (equilibrated successively in buffer D and buffer E + 0.1 mM GTP) and rotated at 7 rpm for 30 min at 4°C. Unbound ^{His6}RUVBL1-RUVBL2 was removed by washing in batch twice with 3 CV of buffer E + 0.1 mM GTP. γTuSC-^{His6}RUVBL1-RUVBL2 was eluted by incubation with 25 μg of 3C protease, rotating at 5 to 7 rpm for 12 to 16 hours at 4°C. Eluted γTuSC-^{His6}RUVBL1-RUVBL2 was centrifuged at 16,100*g* for 10 min at 4°C, either concentrated as described for γTuSC or directly snap-frozen in liquid nitrogen, and stored at −80°C.

γ-Tubulin ring complex

Following multisubunit expression, cell pellets with γTuRC containing GCP6$^{3C–Twin-Strep}$ were resuspended in 5 ml of buffer C + 1× PhosSTOP phosphatase inhibitors (Roche) + 0.1 mM GTP per gram of cell pellet, lysed using a dounce tissue grinder with 20 strokes on ice, and centrifuged for 25 min at 20,000*g* at 4°C. Cleared cell extracts, supplemented with avidin and nuclease as described for γTuSC, were bound by gravity flow to 0.5 ml of equilibrated Strep-Tactin XT resin per liter suspension culture. Resin was washed, and γTuRC was eluted by 3C protease digestion as described for γTuSC. Purified γTuRC was directly used for analysis by sucrose gradient centrifugation. For other analyses, the sample was concentrated by centrifugation in Vivaspin 500 devices (30-kDa MWCO), and centrifuged at 16,100*g* for 10 min at 4°C. Concentrated γTuRC was kept on ice for immediate use or snap-frozen in liquid nitrogen for storage at −80°C. The typical yield was ~0.2 mg of γTuRC per 1.5 liters of expression culture.

Identification of subunits required to reconstitute γTuSC and γTuRC

Small-scale cultures (20 to 50 ml) were infected with a single baculovirus containing subunit combinations as described above. Purifications were carried out as described above for γTuRC with the following modifications. For lysis, cell suspensions were passed five times through a 27-gauge syringe needle (Becton Dickinson). After clearing, proteins were bound to 100 μl of Strep-Tactin XT and purified as described before.

Immunoprecipitation

HEK293T cells were lysed 10 min on ice in lysis buffer [50 mM Hepes (pH 7.4), 150 mM NaCl, 1 mM $MgCl_2$, 1 mM EGTA, and 1% IGEPAL CA-630] + 1× protease inhibitors. After centrifugation for 15 min at 16,000*g* at 4°C, cleared extracts were incubated with anti-FLAG M2 agarose (Sigma-Aldrich) for 2 hours at 4°C. Beads were pelleted, washed three times with lysis buffer, and boiled in Laemmli sample buffer, and the samples were analyzed by SDS-PAGE and Western blotting.

Protein gel electrophoresis and Western blotting

Protein samples in Laemmli buffer were analyzed by SDS-PAGE using 8, 10, or 12% bis-tris polyacrylamide gels. In some cases, to retain MZT1 and MZT2 in the gel matrix with good separation of larger proteins, we prepared 10% gels on top of a 20% gel layer. Proteins were detected by staining with InstantBlue (Expedeon) or by adding 0.5% (v/v) trichloroethanol (Sigma-Aldrich), followed by stain-free imaging using ultraviolet light in a G:BOX F3 (Syngene). For Western blotting, proteins were transferred onto nitrocellulose or polyvinylidene difluoride membranes as described (*17*). GCP2, GCP3, GCP4, GCP, GCP6, MZT1, MZT2, and NEDD1 were detected with custom-made rabbit antibodies (*17*, *20*, *36*). For other proteins, we used mouse anti–γ-tubulin (GTU-88, Sigma-Aldrich), mouse anti-FLAG M2 (F1804, Sigma-Aldrich), mouse anti–glyceraldehyde-3-phosphate dehydrogenase (GAPDH) (sc-47724, Santa Cruz Biotechnology), rabbit anti-RUVBL1 (10210-2-AP, ProteinTech), mouse anti-RUVBL2 (sc-374135, Santa Cruz Biotechnology), and rabbit anti-GFP (TP401, Torrey Pines Biolabs) antibodies.

Chemical cross-linking

γTuSC aliquots stored at −80°C were quickly thawed, centrifuged at 16,100*g* for 10 min at 4°C, and kept on ice. Concentration was adjusted to 1 mg/ml (3 μM, assuming M_r (γTuSC) = 334,892) with freshly degassed buffer E. DSBU was dissolved in dimethyl sulfoxide (DMSO) (liquid chromatography–MS grade, Thermo Fisher Scientific) and added to 180 μg of γTuSC at final concentrations of 150, 300, 600, 1200, and 3000 μM (50×, 100×, 200×, 400×, and 1000× molar excess), mixed, and incubated for 30 min at 20°C. As a control, γTuSC was mixed and incubated with 1 μl of DMSO. Cross-linking was quenched by adding tris (pH 8.0) to a final concentration of 100 mM, followed by incubation for 30 min at 20°C. Aliquots were heated in Laemmli buffer for 5 min at 95°C and analyzed by SDS-PAGE. Coomassie-stained polyacrylamide gels were used for subsequent CL-MS analysis.

Cross-linking mass spectrometry

Protein bands from an 8% polyacrylamide gel were excised, cut into smaller pieces, washed with 50 mM NH_4HCO_3 and acetonitrile (ACN), reduced with 10 mM dithiothreitol, and alkylated with 50 mM iodoacetic acid. γTuSC samples cross-linked with 200× and 1000× molar excess DSBU were digested with Sequencing Grade Modified Trypsin (Promega), the sample cross-linked with 400× molar excess DSBU was digested with chymotrypsin. Digestions were stopped with 5% formic acid (FA) and eluted with ACN. After drying in a

SpeedVac, samples were reconstituted in 20 µl of aqueous solution of 3% ACN and 1% FA. For MS analysis, samples were loaded to a 100 µm by 2 cm Acclaim PepMap100, 5 µm, 100 Å, C18 (Thermo Fisher Scientific) at a flow rate of 15 µl/min using a Dionex UltiMate 3000 chromatographic system (Thermo Fisher Scientific). Peptides were separated using a C18 analytical column (nanoEase MZ HSS T3 column, 75 µm by 250 mm, 1.8 µm, 100 Å, Waters) with a 90-min run, comprising three consecutive steps with linear gradients from 3 to 35% B in 60 min, from 35 to 50% B in 5 min, and from 50 to 85% B in 2 min, followed by isocratic elution at 85% B in 5 min and stabilization to initial conditions (A = 0.1% FA in water and B = 0.1% FA in ACN). The column outlet was directly connected to an Advion TriVersa NanoMate (Advion) fitted on an Orbitrap Fusion Lumos Tribrid (Thermo Fisher Scientific). The mass spectrometer was operated in a data-dependent acquisition mode. Survey MS scans were acquired in the Orbitrap with the resolution (defined at 200 mass/charge ratio) set to 120,000. The highest charge state ions per scan were fragmented in the higher-energy collisional dissociation (HCD) cell and detected in the Orbitrap (30,000 resolution) with stepped collision energies. The ion count target value was 400,000 for the survey scan and 10,000 for the tandem MS (MS/MS) scan. Target ions already selected for MS/MS were dynamically excluded for 15 s. Spray voltage in the NanoMate source was set to 1.70 kV. Radio frequency (RF) lens were tuned to 30%. The spectrometer was working in positive polarity mode, and singly charge state precursors were rejected for fragmentation.

For the proteomics bioinformatics workflow, we devised a multiple software search comprising three cross-linking identifying nodes: XlinkX (v2.2) (*49*) from the Thermo Scientific software Proteome Discoverer (v2.3), MeroX (v2.0.1.1) (*49*), and xiSEARCH (v1.7.4) (*50*). All searches were run against a FASTA database containing γTuSC subunits TUBG1 (P23258), GCP2 (Q9BSJ2), GCP3 (Q96CW5), MZT1 (Q08AG7), and MZT2B (Q6NZ67). The main search parameters for these three nodes were the following: trypsin or chymotrypsin as digesting enzymes allowing two missed cleavage sites (three for MeroX); carbamidomethyl in cysteine as static modification; oxidation in methionine as dynamic modification; DSBU definition as cross-linker between lysine, protein N terminus, and lysine, serine, threonine, tyrosine, and protein C terminus; peptide mass tolerance of 10 parts per million (ppm); MS/MS tolerance of 20 ppm (10 ppm for MeroX); and a false discovery rate of >1% threshold definition. We integrated the three search results in a single harmonized dataset, ready to be visualized with the interactive online tool xiNET (*51*).

In vitro microtubule nucleation assay

Rhodamine-labeled porcine brain tubulin (Cytoskeleton) and unlabeled porcine brain tubulin (*52*) were diluted on ice in assay buffer [80 mM Pipes-KOH (pH 6.9), 2 mM $MgCl_2$, 0.5 mM EGTA, and 1 mM GTP] at a ratio of 1:10 to a final concentration of 50 µM. To remove aggregates, the tubulin mix was centrifuged at 50,000 rpm in a TLA-55 rotor (Beckman Coulter) for 10 min at 4°C. After centrifugation, tubulin concentration was verified by Bradford assay (Bio-Rad). Nucleation assays were set up in PCR tubes in 10 µl of reactions by diluting 1 µl of γTuRC prep (final concentration, ~1 nM) and tubulin stock mix (final concentration, 20 µM) with assay buffer on ice. One microliter of aliquots was taken and mixed with 9 µl of prewarmed fixation buffer [80 mM Pipes-KOH (pH 6.9), 2 mM $MgCl_2$, 0.5 mM EGTA, 50% glycerol, and 0.1% glutaraldehyde] to obtain a "0-min" sample. The assay was started by transferring the reactions to a T100 thermal cycler (Bio-Rad) set to 37°C. After 5 min, 1 µl of aliquots was taken and fixed with fixation buffer. One microliter of fixed reactions of each time point was pipetted on microscope glass slides (Knittel Glass) and covered with 12-mm round coverslips (Thermo Fisher Scientific). Rhodamine-labeled microtubules were imaged by fluorescence microscopy using a DMI6000B microscope (Leica) with 1.4-NA 63× oil immersion objective.

Negative-stain EM of γTuSC complexes

Aliquots of purified γTuSC (2.5 µl) were applied to carbon-coated grids and stained using 1% uranyl acetate. Samples were observed using a FEI Tecnai G2 Spirit with a Lab6 filament and operated at 120 kV. Several hundred micrographs were collected using an automatic low-dose data collection in a TVIPS camera, and particles were extracted. Images were then processed using Relion 3.1 (*53*) and cryoSPARC v2 (*54*). After 2D classification and averaging, we obtained several 2D averages, of which we selected two representative examples containing 4489 particles for γTuSC and 344 particles for an average showing two γTuSCs associated laterally.

Negative-stain EM of RUVBL-γTuSC complexes

The RUVBL-γTuSC complex was assembled by mixing an eightfold excess of γTuSC particles over 0.8 µM hexameric RUVBL1-RUVBL2 in a buffer containing 50 mM Hepes-NaOH (pH 7.5), 200 mM NaCl, 1 mM EGTA, 1 mM $MgCl_2$, and 2 mM β-mercaptoethanol. The complex was stabilized by mild cross-linking using 0.01% (v/v) glutaraldehyde for 1 hour on ice, and the reaction was stopped by adding 40 mM tris-HCl (pH 7). The complex was purified using Ni–nitrilotriacetic acid agarose (Qiagen) beads to bind His-RUVBL1-RUVBL2. The complex was eluted using the same buffer supplemented with 500 mM imidazole, and a few microliters were applied directly to carbon-coated copper grids after glow discharge. The grids were stained using 1% uranyl acetate. We collected 536 micrographs using a FEI Tecnai G2 Spirit with a Lab6 filament and a TVIPS camera. A total of 32,327 particles were extracted and subjected to image processing using Relion 3.1 (*53*) and cryoSPARC v2 (*54*). After classification, representative 2D averages were obtained containing around 200 to 300 particles per average (details in figure legends). Particles were classified in 3D into more homogeneous subgroups, and a subgroup containing 10,455 particles was further refined into a reconstruction at a ~26-Å resolution estimated using the gold-standard criterion and a cutoff of 0.143. The negative-stain structure of RUVBL-γTuSC was interpreted by fitting low-resolution versions of γTuSC and RUVBL obtained by filtering γTuSC from this work, and a RUVBL1-RUVBL2 ATPase hexamer lacking most of the domain II (PDB 2XSZ). Fitting was performed using the sequential fitting tool in University of California San Francisco (UCSF) Chimera without user intervention (*55*). UCSF Chimera fitted copies of γTuSC into each GCP pair of the low-resolution structure, whereas the RUVBL ring was fitted within the extra density.

Cryo-EM of the γTuRC, sample preparation, and image acquisition

Aliquots of purified γTuRC (2.5 µl) were applied to glow discharge holey carbon grids (Quantifoil R1.2/1.3 300–square mesh copper grids) coated with a continuous carbon film. Excess buffer was blotted away, and the sample was vitrified in liquid ethane using a Vitrobot Mark IV (Thermo Fisher Scientific) set to 4°C and 90% humidity.

Cryo-EM grids were stored at liquid nitrogen temperature. Data were collected using EPU software on a 300-kV Titan Krios G3 electron microscope (Thermo Fisher Scientific) using a BioQuantum energy filter (Gatan) and a K3 direct electron detector operated in counting mode. A total of 13,035 movies where collected over two sessions at a pixel size of 0.545 Å per pixel and a defocus range of 1.5- to 3.5-µm underfocus. A total of 1686 movies were collected in the first session, with a total dose of 41.85 $e^-/Å^2$ across 45 frames (0.93 $e^-/Å^2$ per frame). Two larger datasets were collected in a second session (11,349 movies in total) with a total dose of around 58 $e^-/Å^2$ across 90 frames (0.65 $e^-/Å^2$ per frame) (fig. S3 and table S2).

Image processing

Datasets were preprocessed individually and subsequently combined for data alignment, classification, and 3D refinement. Large beam-induced motions were corrected by aligning all movie frames using MotionCor2 and 7 × 5 patches (*56*). Contrast transfer function (CTF) parameters were estimated using Gctf (*57*). Particles were autopicked using Relion 3.1 after creating references from manually selected particles (*53*).

More than 2 million particles were initially selected and binned by a factor of 4 and subjected to reference-free alignment and 2D classification using Relion 3.1 (*53*) and cryoSPARC v2 (*54*). On the basis of 2D classification and averaging, we selected a dataset of 139,143 best quality particles to generate an initial template with the ab initio reconstruction tools in cryoSPARC. This starting reference was used as template for subsequent 3D classification and refinement steps (fig. S3). Further image processing steps were entirely carried out in Relion 3.1. After an initial 3D refinement, CTF parameters, such as beam tilt, magnification anisotropy, particle defocus, and micrographs astigmatism, were refined. After another run of 3D refinement, particles were individually corrected for beam-induced motion using the Bayesian particle polishing tool and subjected to another round of CTF refinement. Following another consensus 3D refinement that included all the selected particles, several rounds of 3D classification were carried out to further improve homogeneity of the dataset by selecting the most homogeneous and best quality particles. A total of 100,182 particles were included in the final refinement of the γTuRC structure. Modulation transfer function correction and B-factor sharpening were carried out using the "postprocessing" protocols in Relion 3.1. The resolution was estimated using the gold-standard criterion and a cutoff of 0.143 (fig. S5). We estimated an average resolution of 4.2 Å, with best resolution regions up to 4.0 Å after local resolution estimations. This revealed the anisotropic resolution of the map, with some regions of the complex notably more flexible than others. Regions with significant differences in their resolution values were segmented, a soft mask was applied to remove the extra density of the complex (particle density subtraction), and focused refinements were conducted (fig. S4). Average resolution and local resolution estimates for each map can be found in fig. S5.

Model building

Subunits in the cryo-EM map were identified independently of the structures of the native complex. γ-Tubulin and the actin-like protein were identified by making use of available crystal structures, and GCPs were detected using the crystal structure of GCP4. The resolution of the actin-like protein in the cryo-EM map was insufficient for modeling, and we fitted the atomic structure of β-actin (PDB 2HF3) as a rigid body. As starting point for modeling of GCPs, the crystal structure of GCP4 (PDB ID 3RIP) (*58*) was fitted in the consensus cryo-EM map, and GCPs were identified by specific structure and sequence features in regions where the resolution was sufficient to confidently fit side chains and by the identification of larger C-terminal regions in GCP3 subunits. Subsequently, homology models for GCP2, GCP3, GCP5, and GCP6 subunits were built with the I-TASSER homology modeling server (*59*), which used information from the previously published structures of the native human γTuRC complex (PDB ID 6V6S) and of GCP4 (PDB ID 3RIP). These models, together with the γ-tubulin crystal structure (PDB ID 3CB2) (*60*), were fitted as rigid bodies into the electron density map (consensus map or subvolumes) using the sequential fitting tool of UCSF Chimera (*55*). The corresponding models for γTuRC stalk-like units, composed of GCP and γ-tubulin, were refined iteratively in real space within subvolumes containing just three γTuRC units with Coot (*61*), Phenix (*62*), and Refmac5 (*63*). Residues absent in the initial homology model that were identified as pertaining to the extra densities observed in the GCP subunits, such as the GCP2 staples and the $GCP6_{1415–1475}$ helices, were manually assigned and refined. Since the resolution of the map in positions 13 and 14 is lower, GCP2, GCP3, and γ-tubulin molecules from positions 7/8 were rigid body-fitted in positions 13/14 using Coot (*61*).

The extra densities corresponding to the staples were clearly connected to the N-terminal density of the closest GCP2 core fold in most of the γTuSC units. To model the structure, we identified this connection and then traced back the backbone up to the staple, fitting the residues and side chains. The resolution was sufficiently high to assign long or bulky side chains, such as K164, K167, K168, F177, W180, Y182, and R184, to the arms of the staple element (Fig. 6D). This also allowed modeling of the loops that connect the two helical arms of the staples.

The C-terminal end of the GCP6 insertion domain contains a helix (residues 1484 to 1510) that connects to the N-terminal end of the second GRIP domain and was partially modeled in the published structure of native human γTuRC (*12*). Our cryo-EM map shows two additional, preceding helices. Although resolution was not sufficient to fit side chains in any of the three helices, we could observe clear connections between all three helices. On the basis of this information and guided by the helical densities of the cryo-EM map and secondary structure predictions by the JPred4 server (*64*), we were able to model the new α helices of residues 1415 to 1439 and 1444 to 1475.

To model the luminal bridge, we first identified three well-connected helices in bundle 2 whose N- and C-terminal helices were not connected to any other density, indicating that they were a separate protein and not part of the GCPs (Fig. 5A, red). A prediction of MTZ1 tertiary structure performed using the I-TASSER server was fitted as rigid body fitting into the cryo-EM density as a start for modeling. Subsequently, the identification of bulky amino acid side chains was used to unequivocally assign the protein sequence of MTZ1 to the model, which was refined in real space with Coot, Phenix, and Refmac. MTZ1 in bundle 2 was embedded within a five-helix bundle that we identified as GCP3 NTEs as follows.

The connectivity between the five helices of the bundle in the cryo-EM map was identified using denoising and sharpening tools. Helix H5 in the bundle was identified in the cryo-EM map of bundle 2 as the short C-terminal helix in closer contact with MTZ1 (Fig. 5B). H5 has been predicted in GCP3, GCP5, and GCP6 as a

short helix containing the MTZ1-binding motif (Fig. 5E) (*17*). This motif contains residues with large side chains, W90 and Y95 in GCP3, Y108 in GCP5, but none in GCP6. Residues at the immediate N- and C-terminal ends of H5 do not have large side chains in any of the three proteins. Since H5 is not very long and the resolution in the cryo-EM density was sufficiently high to identify large side chains, we were able to assign H5 as GCP3. Cryo-EM density of H5 in bundle 2 shows two prominent side chains that could only be fitted by W90 and Y95 in GCP3 (arrowheads in Fig. 5E, right). Then, we were able to build a model for the remaining helices of the bundle, and the good agreement of large side chains with the cryo-EM density corroborated the assignment (Fig. 5F, H2 as example). Bundle 1 was found to be very similar to bundle 2 after a 180° rotation, and this was used to identify a second molecule of MTZ1. Using similar procedures to those described for bundle 2, we identified H5 in this bundle as GCP6 because large side chains of residues Y95 and W90 in GCP3 and Y108 in GCP5 (arrowheads in Fig. 5E, left) could not be accommodated in the density, whereas H5 in GCP6 lacks residues with large side chains (Fig. 5E). Then, we modeled the remaining helices confirming this assignment thanks to the good agreement of side chains and the cryo-EM map (Fig. 5F, H4 as example). During preparation of this manuscript, structures of the bundles in the luminal bridge were published, and our model and register of helices agree with the published structures (*21*, *44*). For bundle 1, resolution of the map did not allow modeling of helices H1 and H2, and these were left as a poly-alanine model.

SUPPLEMENTARY MATERIALS

Supplementary material for this article is available at http://advances.sciencemag.org/cgi/content/full/6/51/eabe0894/DC1

View/request a protocol for this paper from *Bio-protocol*.

REFERENCES AND NOTES

1. J. Paz, J. Lüders, Microtubule-organizing centers: Towards a minimal parts list. *Trends Cell Biol.* **28**, 176–187 (2018).
2. A. D. Sanchez, J. L. Feldman, Microtubule-organizing centers: From the centrosome to non-centrosomal sites. *Curr. Opin. Cell Biol.* **44**, 93–101 (2017).
3. C. A. Tovey, P. T. Conduit, Microtubule nucleation by γ-tubulin complexes and beyond. *Essays Biochem.* **62**, 765–780 (2018).
4. D. Farache, L. Emorine, L. Haren, A. Merdes, Assembly and regulation of γ-tubulin complexes. *Open Biol.* **8**, 170266 (2018).
5. J. M. Kollman, A. Zelter, E. G. D. Muller, B. Fox, L. M. Rice, T. N. Davis, D. A. Agard, The structure of the γ-tubulin small complex: Implications of its architecture and flexibility for microtubule nucleation. *Mol. Biol. Cell* **19**, 207–215 (2008).
6. Y. Zheng, M. L. Wong, B. Alberts, T. Mitchison, Nucleation of microtubule assembly by a γ-tubulin-containing ring complex. *Nature* **378**, 578–583 (1995).
7. M. Moritz, M. B. Braunfeld, J. W. Sedat, B. Alberts, D. A. Agard, Microtubule nucleation by γ-tubulin-containing rings in the centrosome. *Nature* **378**, 638–640 (1995).
8. M. Moritz, M. B. Braunfeld, V. Guénebaut, J. Heuser, D. A. Agard, Structure of the γ-tubulin ring complex: A template for microtubule nucleation. *Nat. Cell Biol.* **2**, 365–370 (2000).
9. S. Erlemann, A. Neuner, L. Gombos, R. Gibeaux, C. Antony, E. Schiebel, An extended γ-tubulin ring functions as a stable platform in microtubule nucleation. *J. Cell Biol.* **197**, 59–74 (2012).
10. J. M. Kollman, J. K. Polka, A. Zelter, T. N. Davis, D. A. Agard, Microtubule nucleating γ-TuSC assembles structures with 13-fold microtubule-like symmetry. *Nature* **466**, 879–882 (2010).
11. J. M. Kollman, C. H. Greenberg, S. Li, M. Moritz, A. Zelter, K. K. Fong, J.-J. Fernandez, A. Sali, J. Kilmartin, T. N. Davis, D. A. Agard, Ring closure activates yeast γTuRC for species-specific microtubule nucleation. *Nat. Struct. Mol. Biol.* **22**, 132–137 (2015).
12. M. Wieczorek, L. Urnavicius, S.-C. Ti, K. R. Molloy, B. T. Chait, T. M. Kapoor, Asymmetric molecular architecture of the human γ-tubulin ring complex. *Cell* **180**, 165–175.e16 (2020).
13. T. Consolati, J. Locke, J. Roostalu, Z. A. Chen, J. Gannon, J. Asthana, W. M. Lim, F. Martino, M. A. Cvetkovic, J. Rappsilber, A. Costa, T. Surrey, Microtubule nucleation properties of single human γTuRCs explained by their Cryo-EM structure. *Dev. Cell* **53**, 603–617.e8 (2020).
14. P. Liu, E. Zupa, A. Neuner, A. Böhler, J. Loerke, D. Flemming, T. Ruppert, T. Rudack, C. Peter, C. Spahn, O. J. Gruss, S. Pfeffer, E. Schiebel, Insights into the assembly and activation of the microtubule nucleator γ-TuRC. *Nature* **578**, 467–471 (2020).
15. Y.-K. Choi, P. Liu, S. K. Sze, C. Dai, R. Z. Qi, CDK5RAP2 stimulates microtubule nucleation by the γ-tubulin ring complex. *J. Cell Biol.* **191**, 1089–1095 (2010).
16. A. Thawani, R. S. Kadzik, S. Petry, XMAP215 is a microtubule nucleation factor that functions synergistically with the γ-tubulin ring complex. *Nat. Cell Biol.* **20**, 575–585 (2018).
17. R. R. Cota, N. Teixidó-Travesa, A. Ezquerra, S. Eibes, C. Lacasa, J. Roig, J. Lüders, MZT1 regulates microtubule nucleation by linking γTuRC assembly to adapter-mediated targeting and activation. *J. Cell Sci.* **130**, 406–419 (2017).
18. T.-C. Lin, A. Neuner, D. Flemming, P. Liu, T. Chinen, U. Jäkle, R. Arkowitz, E. Schiebel, MOZART1 and γ-tubulin complex receptors are both required to turn γ-TuSC into an active microtubule nucleation template. *J. Cell Biol.* **215**, 823–840 (2016).
19. S. L. Leong, E. M. Lynch, J. Zou, Y. D. Tay, W. E. Borek, M. W. Tuijtel, J. Rappsilber, K. E. Sawin, Reconstitution of microtubule nucleation in vitro reveals novel roles for Mzt1. *Curr. Biol.* **29**, 2199–2207.e10 (2019).
20. N. Teixidó-Travesa, J. Villén, C. Lacasa, M. T. Bertran, M. Archinti, S. P. Gygi, C. Caelles, J. Roig, J. Lüders, The γTuRC revisited: A comparative analysis of interphase and mitotic human γTuRC redefines the set of core components and identifies the novel subunit GCP8. *Mol. Biol. Cell* **21**, 3963–3972 (2010).
21. M. Wieczorek, T.-L. Huang, L. Urnavicius, K.-C. Hsia, T. M. Kapoor, MZT proteins form multi-faceted structural modules in the γ-tubulin ring complex. *Cell Rep.* **31**, 107791 (2020).
22. N. Teixidó-Travesa, J. Roig, J. Lüders, The where, when and how of microtubule nucleation – One ring to rule them all. *J. Cell Sci.* **125**, 4445–4456 (2012).
23. J. R. A. Hutchins, Y. Toyoda, B. Hegemann, I. Poser, J.-K. Hériché, M. M. Sykora, M. Augsburg, O. Hudecz, B. A. Buschhorn, J. Bulkescher, C. Conrad, D. Comartin, A. Schleiffer, M. Sarov, A. Pozniakovsky, M. M. Slabicki, S. Schloissnig, I. Steinmacher, M. Leuschner, A. Ssykor, S. Lawo, L. Pelletier, H. Stark, K. Nasmyth, J. Ellenberg, R. Durbin, F. Buchholz, K. Mechtler, A. A. Hyman, J.-M. Peters, Systematic analysis of human protein complexes identifies chromosome segregation proteins. *Science* **328**, 593–599 (2010).
24. R. Melki, I. E. Vainberg, R. L. Chow, N. J. Cowan, Chaperonin-mediated folding of vertebrate actin-related protein and γ-tubulin. *J. Cell Biol.* **122**, 1301–1310 (1993).
25. F. Martino, M. Pal, H. Muñoz-Hernández, C. F. Rodríguez, R. Núñez-Ramírez, D. Gil-Carton, G. Degliesposti, J. M. Skehel, S. M. Roe, C. Prodromou, L. H. Pearl, O. Llorca, RPAP3 provides a flexible scaffold for coupling HSP90 to the human R2TP co-chaperone complex. *Nat. Commun.* **9**, 1501 (2018).
26. W. A. Houry, E. Bertrand, B. Coulombe, The PAQosome, an R2TP-based chaperone for quaternary structure formation. *Trends Biochem. Sci.* **43**, 4–9 (2018).
27. H. Muñoz-Hernández, M. Pal, C. F. Rodríguez, C. Prodromou, L. H. Pearl, O. Llorca, Advances on the structure of the R2TP/Prefoldin-like complex. *Adv. Exp. Med. Biol.* **1106**, 73–83 (2018).
28. D. Ducat, S.-i. Kawaguchi, H. Liu, J. R. Yates, Y. Zheng, Regulation of microtubule assembly and organization in mitosis by the AAA+ ATPase pontin. *Mol. Biol. Cell* **19**, 3097–3110 (2008).
29. W. Gartner, J. Rossbacher, B. Zierhut, T. Daneva, W. Base, M. Weissel, W. Waldhäusl, M. S. Pasternack, L. Wagner, The ATP-dependent helicase RUVBL1/TIP49a associates with tubulin during mitosis. *Cell Motil. Cytoskeleton* **56**, 79–93 (2003).
30. S. Eustermann, K. Schall, D. Kostrewa, K. Lakomek, M. Strauss, M. Moldt, K.-P. Hopfner, Structural basis for ATP-dependent chromatin remodelling by the INO80 complex. *Nature* **556**, 386–390 (2018).
31. O. Willhoft, M. Ghoneim, C.-L. Lin, E. Y. D. Chua, M. Wilkinson, Y. Chaban, R. Ayala, E. A. McCormack, L. Ocloo, D. S. Rueda, D. B. Wigley, Structure and dynamics of the yeast SWR1-nucleosome complex. *Science* **362**, eaat7716 (2018).
32. N. J. Watkins, I. Lemm, D. Ingelfinger, C. Schneider, M. Hoßbach, H. Urlaub, R. Lührmann, Assembly and maturation of the U3 snoRNP in the nucleoplasm in a large dynamic multiprotein complex. *Mol. Cell* **16**, 789–798 (2004).
33. L. Haren, D. Farache, L. Emorine, A. Merdes, A stable sub-complex between GCP4, GCP5 and GCP6 promotes the assembly of γ-tubulin ring complexes. *J. Cell Sci.* **133**, jcs244368 (2020).
34. R. Bahtz, J. Seidler, M. Arnold, U. Haselmann-Weiss, C. Antony, W. D. Lehmann, I. Hoffmann, GCP6 is a substrate of Plk4 and required for centriole duplication. *J. Cell Sci.* **125** (Pt. 2), 486–496 (2012).
35. L. Haren, M.-H. Remy, I. Bazin, I. Callebaut, M. Wright, A. Merdes, NEDD1-dependent recruitment of the γ-tubulin ring complex to the centrosome is necessary for centriole duplication and spindle assembly. *J. Cell Biol.* **172**, 505–515 (2006).
36. J. Lüders, U. K. Patel, T. Stearns, GCP-WD is a γ-tubulin targeting factor required for centrosomal and chromatin-mediated microtubule nucleation. *Nat. Cell Biol.* **8**, 137–147 (2006).
37. D. K. Dhani, B. T. Goult, G. M. George, D. T. Rogerson, D. A. Bitton, C. J. Miller, J. W. R. Schwabe, K. Tanaka, Mzt1/Tam4, a fission yeast MOZART1 homologue, is

an essential component of the γ-tubulin complex and directly interacts with GCP3^{Alp6}. *Mol. Biol. Cell* **24**, 3337–3349 (2013).
38. N. Janski, K. Masoud, M. Batzenschlager, E. Herzog, J.-L. Evrard, G. Houlné, M. Bourge, M.-E. Chabouté, A.-C. Schmit, The GCP3-interacting proteins GIP1 and GIP2 are required for γ-tubulin complex protein localization, spindle integrity, and chromosomal stability. *Plant Cell* **24**, 1171–1187 (2012).
39. M. Q. Müller, F. Dreiocker, C. H. Ihling, M. Schäfer, A. Sinz, Cleavable cross-linker for protein structure analysis: Reliable identification of cross-linking products by tandem MS. *Anal. Chem.* **82**, 6958–6968 (2010).
40. X.-c. Bai, E. Rajendra, G. Yang, Y. Shi, S. H. W. Scheres, Sampling the conformational space of the catalytic subunit of human γ-secretase. *eLife* **4**, e11182 (2015).
41. M. Batzenschlager, K. Masoud, N. Janski, G. Houlné, E. Herzog, J.-L. Evrard, N. Baumberger, M. Erhardt, Y. Nominé, B. Kieffer, A.-C. Schmit, M.-E. Chabouté, The GIP gamma-tubulin complex-associated proteins are involved in nuclear architecture in *Arabidopsis thaliana*. *Front. Plant Sci.* **4**, 480 (2013).
42. C. D. Cukier, A. Tourdes, D. El-Mazouni, V. Guillet, J. Nomme, L. Mourey, A. Milon, A. Merdes, V. Gervais, NMR secondary structure and interactions of recombinant human MOZART1 protein, a component of the gamma-tubulin complex. *Protein Sci.* **26**, 2240–2248 (2017).
43. A. Thawani, M. J. Rale, N. Coudray, G. Bhabha, H. A. Stone, J. W. Shaevitz, S. Petry, The transition state and regulation of γ-TuRC-mediated microtubule nucleation revealed by single molecule microscopy. *eLife* **9**, e54253 (2020).
44. T.-L. Huang, H.-J. Wang, Y.-C. Chang, S.-W. Wang, K.-C. Hsia, Promiscuous binding of microprotein mozart1 to γ-tubulin complex mediates specific subcellular targeting to control microtubule array formation. *Cell Rep.* **31**, 107836 (2020).
45. C. F. Rodríguez, O. Llorca, RPAP3 C-terminal domain: A conserved domain for the assembly of R2TP co-chaperone complexes. *Cell* **9**, 1139 (2020).
46. F. Weissmann, J.-M. Peters, Expressing multi-subunit complexes using biGBac. *Methods Mol. Biol.* **1764**, 329–343 (2018).
47. J. Scholz, S. Suppmann, A new single-step protocol for rapid baculovirus-driven protein production in insect cells. *BMC Biotechnol.* **17**, 83 (2017).
48. A. López-Perrote, H. Muñoz-Hernández, D. Gil, O. Llorca, Conformational transitions regulate the exposure of a DNA-binding domain in the RuvBL1–RuvBL2 complex. *Nucleic Acids Res.* **40**, 11086–11099 (2012).
49. C. Iacobucci, M. Götze, C. H. Ihling, C. Piotrowski, C. Arlt, M. Schäfer, C. Hage, R. Schmidt, A. Sinz, A cross-linking/mass spectrometry workflow based on MS-cleavable cross-linkers and the MeroX software for studying protein structures and protein-protein interactions. *Nat. Protoc.* **13**, 2864–2889 (2018).
50. M. L. Mendes, L. Fischer, Z. A. Chen, M. Barbon, F. J. O'Reilly, S. H. Giese, M. Bohlke Schneider, A. Belsom, T. Dau, C. W. Combe, M. Graham, M. R. Eisele, W. Baumeister, C. Speck, J. Rappsilber, An integrated workflow for crosslinking mass spectrometry. *Mol. Syst. Biol.* **15**, e8994 (2019).
51. C. W. Combe, L. Fischer, J. Rappsilber, xiNET: Cross-link network maps with residue resolution. *Mol. Cell. Proteomics* **14**, 1137–1147 (2015).
52. R. B. Vallee, Reversible assembly purification of microtubules without assembly-promoting agents and further purification of tubulin, microtubule-associated proteins, and MAP fragments. *Methods Enzymol.* **134**, 89–104 (1986).
53. J. Zivanov, T. Nakane, B. O. Forsberg, D. Kimanius, W. J. H. Hagen, E. Lindahl, S. H. W. Scheres, New tools for automated high-resolution cryo-EM structure determination in RELION-3. *eLife* **7**, e42166 (2018).
54. A. Punjani, J. L. Rubinstein, D. J. Fleet, M. A. Brubaker, cryoSPARC: Algorithms for rapid unsupervised cryo-EM structure determination. *Nat. Methods* **14**, 290–296 (2017).
55. E. F. Pettersen, T. D. Goddard, C. C. Huang, G. S. Couch, D. M. Greenblatt, E. C. Meng, T. E. Ferrin, UCSF Chimera—A visualization system for exploratory research and analysis. *J. Comput. Chem.* **25**, 1605–1612 (2004).
56. S. Q. Zheng, E. Palovcak, J.-P. Armache, K. A. Verba, Y. Cheng, D. A. Agard, MotionCor2: Anisotropic correction of beam-induced motion for improved cryo-electron microscopy. *Nat. Methods* **14**, 331–332 (2017).
57. K. Zhang, Gctf: Real-time CTF determination and correction. *J. Struct. Biol.* **193**, 1–12 (2016).
58. V. Guillet, M. Knibiehler, L. Gregory-Pauron, M.-H. Remy, C. Chemin, B. Raynaud-Messina, C. Bon, J. M. Kollman, D. A. Agard, A. Merdes, L. Mourey, Crystal structure of γ-tubulin complex protein GCP4 provides insight into microtubule nucleation. *Nat. Struct. Mol. Biol.* **18**, 915–919 (2011).
59. J. Yang, Y. Zhang, I-TASSER server: New development for protein structure and function predictions. *Nucleic Acids Res.* **43**, W174–W181 (2015).
60. L. M. Rice, E. A. Montabana, D. A. Agard, The lattice as allosteric effector: Structural studies of αβ- and γ-tubulin clarify the role of GTP in microtubule assembly. *Proc. Natl. Acad. Sci. U.S.A.* **105**, 5378–5383 (2008).
61. P. Emsley, B. Lohkamp, W. G. Scott, K. Cowtan, Features and development of *Coot*. *Acta Crystallogr. D Biol. Crystallogr.* **66** (Pt. 4), 486–501 (2010).
62. P. D. Adams, P. V. Afonine, G. Bunkóczi, V. B. Chen, I. W. Davis, N. Echols, J. J. Headd, L.-W. Hung, G. J. Kapral, R. W. Grosse-Kunstleve, A. J. McCoy, N. W. Moriarty, R. Oeffner, R. J. Read, D. C. Richardson, J. S. Richardson, T. C. Terwilliger, P. H. Zwart, *PHENIX*: A comprehensive Python-based system for macromolecular structure solution. *Acta Crystallogr. D Biol. Crystallogr.* **66** (Pt. 2), 213–221 (2010).
63. G. N. Murshudov, P. Skubák, A. A. Lebedev, N. S. Pannu, R. A. Steiner, R. A. Nicholls, M. D. Winn, F. Long, A. A. Vagin, *REFMAC5* for the refinement of macromolecular crystal structures. *Acta Crystallogr. D Biol. Crystallogr.* **67** (Pt. 4), 355–367 (2011).
64. A. Drozdetskiy, C. Cole, J. Procter, G. J. Barton, JPred4: A protein secondary structure prediction server. *Nucleic Acids Res.* **43**, W389–W394 (2015).
65. E. Krissinel, K. Henrick, Inference of macromolecular assemblies from crystalline state. *J. Mol. Biol.* **372**, 774–797 (2007).

Acknowledgments: RUVBL1 and RUVBL2 cDNAs codon-optimized for insect cell expression were a gift from D. Wigley (Imperial College, London, UK). We are grateful to A. S. Jijumon and C. Janke (Institut Curie, Paris, France) for hosting F.Z. and providing experimental expertise on tubulin purification as well as providing purified pig brain tubulin. We thank C. Savva (University of Leicester, UK) for cryo-EM data collection, J. Boskovic and C. G. Martín for support at CNIO Electron Microscopy Facilities, and E. Arias-Palomo (CIB-CSIC, Madrid) for help in preparing carbon-coated grids. **Funding:** The following funding is acknowledged: Support to J.L. by grants BFU2015-69275-P (MINECO/FEDER), PGC2018-099562-B-I00 (MICINN), 2017 SGR 1089 (AGAUR), and by IRB Barcelona intramural funds. SAF2017-82632-P to O.L. by the Spanish Ministry of Science, Innovation and Universities (MCIU/AEI), co-funded by the European Regional Development Fund (ERDF); the support of the National Institute of Health Carlos III to CNIO; projects Y2018/BIO4747 and P2018/NMT4443 from the Autonomous Region of Madrid and co-funded by the European Social Fund and the European Regional Development Fund to the activities of the group directed by O.L. F.Z. was supported by a fellowship from the "la Caixa" Foundation (ID 100010434, fellowship code LCF/BQ/DI17/11620020) and the European Union's Horizon 2020 research and innovation program under the Marie Skłodowska-Curie grant agreement no. 713673. We thank the IRB Mass Spectrometry & Proteomics Core Facility, a member of ProteoRed, PRB3-ISCIII, supported by grant PRB3 (IPT17/0019 - ISCIIISGEFI/ERDF), for excellent support and the IRB Protein Expression Core Facility for purified 3C protease, cloning, and valuable advice. **Author contributions:** F.Z. performed all cell and biochemical experiments, including purifications except recombinant RUVBL, which was purified by M.S. A.E. mapped the MZT2 binding region in GCP2. M.S. performed all EM and cryo-EM experiments, image processing, and model building. R.F.-L. helped during image processing and modeling. O.L. and J.L. designed the research and prepared the manuscript. F.Z. and M.S., with contributions from O.L. and J.L., prepared figures and revised the manuscript. **Competing interest:** The authors declare that they have no competing interests. **Data and materials availability:** The cryo-EM maps and the atomic model of the recombinant γTuRC were deposited in the EMDB/PDB. All accession codes are indicated in table S2. All other data needed to evaluate the conclusions in the paper are presented in the paper and/or the Supplementary Materials. Additional data related to this paper may be requested from the authors.

Submitted 30 July 2020
Accepted 11 November 2020
Published 18 December 2020
10.1126/sciadv.abe0894

Citation: F. Zimmermann, M. Serna, A. Ezquerra, R. Fernandez-Leiro, O. Llorca, J. Luders, Assembly of the asymmetric human γ-tubulin ring complex by RUVBL1-RUVBL2 AAA ATPase. *Sci. Adv.* **6**, eabe0894 (2020).